- pyShore: A deep learning toolkit for shoreline structure mapping
- with high-resolution orthographic imagery and convolutional
- neural networks
- ⁴ Zhonghui Lv^{a,b}, Karinna Nunez^a, Ethan Brewer^{b,c} and Dan Runfola^b
- ^aCenter for Coastal Resource Management, Virginia Institute of Marine Science, William and Mary
- 6 bDepartment of Applied Science, William and Mary
- ^cDepartment of Computer Science and Engineering, New York University

ARTICLE INFO

Keywords:

11

12

15

16

17 18

19

20

21

22

23

26

13 deep learning

coastal management

remote sensing

semantic segmentation

ABSTRACT

The process of mapping shoreline structures (i.e., riprap, groins, breakwaters or bulkheads) is heavily reliant on in-situ field surveys and manual delineation using orthoimagery or aerial imagery. These processes are time and resource intensive, resulting in update times of longer than a decade for larger waterbodies. In this study, we explore the effectiveness of a deep learning approach to map shoreline armoring structures from remotely sensed high-resolution imagery. We focus on computationally efficient techniques which can be deployed in desktop environments similar to those used by human coders today, with the goal of providing a semi-automated technique which reduces the total amount of time required to delineate shoreline structures. We test a range of architectures using a dataset of over 10,000 observations of four classes of shoreline structure, finding that a ResNet18 based Pyramid Attention Network (PAN) architecture achieves 72% overall accuracy (60 cm resolution), with 80% and 94% prediction accuracy in breakwater and groins, respectively. This relatively lightweight implementation enabled a 1.5 kilometers of shoreline to be processed in 1.4 seconds (GPU) to 2.16 seconds (CPU) in simulated user environments. Finally, we present pyShore, an implementation of this deep learning algorithm made available for human coders to apply as a part of a semi-automated workflow.

CRediT authorship contribution statement

Zhonghui Lv: conceptualized the project, selected and refined relevant algorithms, algorithmic development,
data preparation and testing, drafted the paper. Karinna Nunez: conceptualized the project, and paper editing. Ethan
Brewer: data and paper editing. Dan Runfola: conceptualized the project, selected and refined relevant algorithms,
and paper editing.

1. Introduction & Related Work

- Maintaining a current inventory of shoreline structures is essential to assessing shoreline stabilization and the health
- of nearshore habitats (Berman and Hershner, 1999; Nunez et al., 2020). Shoreline hardening structures that protect
- upland property from erosion act not only as barriers which inhibit marsh migration (Titus et al., 2009; Gittman et al.,
- 2015; Hill, 2015; Enwright et al., 2016), but also represent barriers for sediment exchange between the marsh habitat
- and the upland (Hill, 2015). Data on the location and nature of shoreline structures is thus an important element in
- coastline management strategies (Nunez et al., 2022; Enwright et al., 2016; Hill, 2015; Gittman et al., 2015; Titus et al.,
- 40 2009).
- Today, this data is primarily provided by shoreline inventory reports generated by government bodies (for example,

ORCID(s): 0000-0001-5186-3699 (Z. Lv)

in the United States these are produced by the state of Virginia (CCRM, 2019), Delaware (Berman et al., 2013), Washington (State of Washington, 2009) and others (Fontenault et al., 2013; MGS, 2000)). These reports describe a range of shoreline structures, including erosion control structures such as riprap, bulkheads, and breakwaters; structures such as groins, designed to accumulate sand in transport; and recreational structures, built to enhance public or private use of the water (CCRM, 2019; Fontenault et al., 2013).

The traditional approach to collecting and mapping shoreline structures consists of a GPS field survey to collect 47 coordinates and attribute information of coastal structures, and then manually delineating the structures and extracting basic feature information (e.g., type, material, and length) from remotely sensed data or other available digital images (CCRM, 2019; Fontenault et al., 2013). These processes require time-intensive in-situ surveys and well-trained technicians to carry them out. For example, the latest shoreline inventory for Virginia was a 12-year process (from 2007 to 2019), including in-situ surveys by trained fieldworkers as well as image digitization by experts. This process resulted in updated historic shoreline reports for Virginia and new inventories in locations with no historic information (CCRM, 2019). As another example of the cost of such efforts, the first Massachusetts Inventory of Publically-owned Coastal Infrastructure was collected over a eight-year period beginning in 2002 using a similar approach including GPS field surveys and desktop interpretation of remotely sensed imagery. In this case, the in-situ survey work took 5 years, while the digitization and GIS data production stage took 3 years of effort (Fontenault et al., 2013). While this approach to assessing the coastal shoreline inventory can generate spatially explicit and highly-resolved outputs, the decade-long process of generating such information can also inhibit contemporary accuracy as shoreline structures are removed or added due to shoreline erosion, sea-level rise, or construction (Gittman et al., 2015; Enwright et al., 2016). This can produce a large gap between the generated data product and the real-world shoreline structure topography (Niculescu et al., 2021).

Over the past three decades, a variety of different techniques have been developed for the extraction of shoreline 63 from remotely sensed imagery. Imagery sources used in the literature range from coarse resolution (Bagli and Soille, 2004; Ghorai and Mahapatra, 2020; Kuleli et al., 2011; Spinosa et al., 2021) to high-resolution (Sekovski et al., 2014; 65 Tarmizi et al., 2014), and include LiDAR-derived data (Palaseanu-Lovejoy et al., 2016; Eboigbe et al., 2020; Liu et al., 66 2011), Synthetic Aperture Radar (SAR) imagery (Mason and Davenport, 1996; Spinosa et al., 2021), and Multispectral 67 Satellite Imagery (MSI) (Sekovski et al., 2014). A common methodology includes classification of pixels in satellite 68 imagery to segment the image into different features (Bagli and Soille, 2004; Di et al., 2003; Kuleli et al., 2011), then using machine learning (Kumar et al., 2020; McAllister et al., 2022a) or threshold analysis (Kuleli et al., 2011; 70 Ghorai and Mahapatra, 2020; Mason and Davenport, 1996) to classify the features into different categories of land or water body, extracting the shorelines from the boundaries between the two. During analysis of the data, techniques such as image enhancement (adjustment of brightness and contrast of individual features (Loos and Niemann, 2002)),

edge detection (Mason and Davenport, 1996; Loos and Niemann, 2002; Kumar et al., 2020; Spinosa et al., 2021),
morphological operations (Spinosa et al., 2021; Ghorai and Mahapatra, 2020), water indexing (Ghorai and Mahapatra,
2020; McAllister et al., 2022b), and GIS processing (Ghorai and Mahapatra, 2020; Zarillo et al., 2008) may be applied
to improve the primary technique and achieve higher accuracy.

Some studies use object-based image analysis (OBIA) which first groups individual pixels into groups of pixels likely reflective of the same objects using a range of algorithms (McAllister et al., 2022a; Gong et al., 2013), treating the grouped pixels as the unit of analysis. The spectral information of the grouped pixels, shapes, texture, and other topological features are then used to classify the segments into different categories (McAllister et al., 2022b; Niculescu et al., 2021). Application-specific tools and metrics are also commonly developed such as beachtool (Zarillo et al., 2008) to extract shoreline locations, and cliffmetric to extract cliffs in coastal areas (Liu et al., 2011; Payo et al., 2018). However, to date the existing literature has focused on the extraction of shorelines from satellite images — to our knowledge, no studies have focused on automatically extracting different types of shoreline armoring structures, the focus of this study.

In this context, the automatic delineation of shoreline armoring structure based on orthographic imagery can help to "fill in the gaps" between in-situ survey efforts, as well as provide more temporally-explicit information on the creation and removal of coastal features. Such automated delineation would benefit many different research fields, including hazard management and mitigation, coastal vulnerability and erosion assessment, environmental risk analysis, and coastal spatial planning and management.

Advances in computer vision for remote sensing applications suggest promise for shoreline structure detection algorithms. In recent years, object detection via remotely sensed images has received considerable attention due to the availability of Very High-Resolution (VHR; i.e., sub-meter) and multispectral sensors (NOAA, 2018; DigitalGlobe, 2018). Since 2012, orthographic imagery analysis using deep learning methods, specifically convolutional neural networks (CNNs) has grown in popularity (Krizhevsky et al., 2012). Recent examples of the use of CNNs with orthoimagery include the detection of buildings (Yang et al., 2017), roads (Brewer et al., 2021; Narayan et al., 2017), 97 marine debris (Kikaki et al., 2022), coastal vegetation mapping (Li et al., 2021; Guirado et al., 2017), landuse mapping 98 (Bhosle and Musande, 2019), and other types of analysis and applications (Runfola et al., 2022, 2021; Goodman et al., aa 2021; Brewer et al., 2022). The wide range of applications of deep learning techniques more broadly have driven a 100 number of research groups to explore ways to tailor approaches to orthoimagery, with a wide range of modeling ap-101 proaches being promoted in recent years (Runfola, 2022; Wang et al., 2022; An et al., 2021; Roberts et al., 2022; Tran 102 et al., 2022; Aravena Pelizari et al., 2021). 103

In this study, we compare multiple state-of-the-art deep learning techniques, specifically an adapted U-Net architecture (Ronneberger et al., 2015), DeeplabV3 (Chen et al., 2016), and Pyramid Attention Network (PAN) (Li et al.,

104

2018) to estimate the spatial location of shoreline structures using high resolution orthographic imagery. The proposed methodology will advance shoreline inventory protocols by identifying and mapping shoreline structures at a regional scale, but with a high spatially explicit resolution within an efficient time frame. We specifically seek to introduce a technique that can be used as a part of a semi-automated pipeline for shoreline inventory collection, aiding individuals digitizing orthoimagery in delineating line features more efficiently than would be feasible without automated shoreline feature detection.

Our paper is organized as follows: in section 1.1 ("Related Work"), we provide a brief overview of relevant literature on mapping and detection tasks, including structure detection, using orthoimagery and deep neural networks (DNNs).

In section 2 ("Material & Methods"), we discuss the data and technical approach we use in the experiment. We introduce our results and provide a discussion in sections 3 and 4. In the discussion, we further present a semi-automated toolkit, *pyShore*, for shoreline armoring structure classification in the ArcGIS Pro software with a user-friendly interface to facilitate the data collection of future work (section 4.5). Finally, we provide a brief conclusion summarizing our findings in section 5.

1.1. Related Work

119

132

133

134

135

136

A significant body of literature exists on the use of segmentation and object detection algorithms with remotely 120 sensed imagery (for a review, see Cheng and Han (2016)). Object detection algorithms have been applied for detection 121 and extraction of features of interest including roads (Wan et al., 2021), buildings (Etten et al., 2021), and vehicles 122 (Chen et al., 2014). Several issues - such as varying size, background, and orientation of target objects - make the 123 automatic detection of features in remotely sensed imagery a challenging problem (Brewer et al., 2022; Bhil et al., 124 2022). Over the past few years, U-Nets (Ronneberger et al., 2015), and variants of region-based convolutional neural 125 networks (R-CNNs) (He et al., 2017), have become popular deep neural network (DNN) based approaches for object detection and segmentation in the greater computer vision community, including within the computer vision remote sensing (CVRS) domain. Some examples of the use of deep learning architectures in CVRS include building detection from high-resolution multispectral imagery (Prathap and Afanasyev, 2018), and building footprint and road detection within OpenStreetMap (OSM) fused with Sentinel-1 and 2 imagery (Ayala et al., 2021).

A small number of studies have been conducted extending specifically to marine science. In 2021, Li et al. employed a U-Net and developed an adaptive deep learning approach to map salt marshes in estuarine emergent wetlands in South Carolina, USA from 20 Sentinel-2 images with an accuracy of 90% (Li et al., 2021). In 2022, marine debris was identified from sentinel-2 imagery using a random forest model (Breiman, 2001) and a deep learning architecture (Kikaki et al., 2022). Other work has explored the effectiveness of deep learning to identify marine objects such as ships (Stofa et al., 2020) and whales (81% detection accuracy) (Guirado et al., 2019). No work to-date has explored

shoreline structure detection from remotely sensed imagery using deep learning, the topic of this article.

38 2. Material & Methods

2.1. Study area

145

146

In this study, we focus on 17,239 kilometers of shoreline located in the state of Virginia in the United States (see Figure 1). The majority of this shoreline surrounds the Chesapeake Bay, a protected estuary responsible for over a hundred billion US dollars of economic output every year, predominantly related to commercial fishing, tourism, recreation, and timber (Phillips and McGee, 2014). The Chesapeake Bay is a focus of estuary protection and renewal activities from the State of Virginia, and also many US federal agencies (Phillips and McGee, 2014). It is further a region with multiple climate mitigation efforts to protect both natural and human built structures (Najjar et al., 2010; Toft et al., 2017; Du et al., 2016).

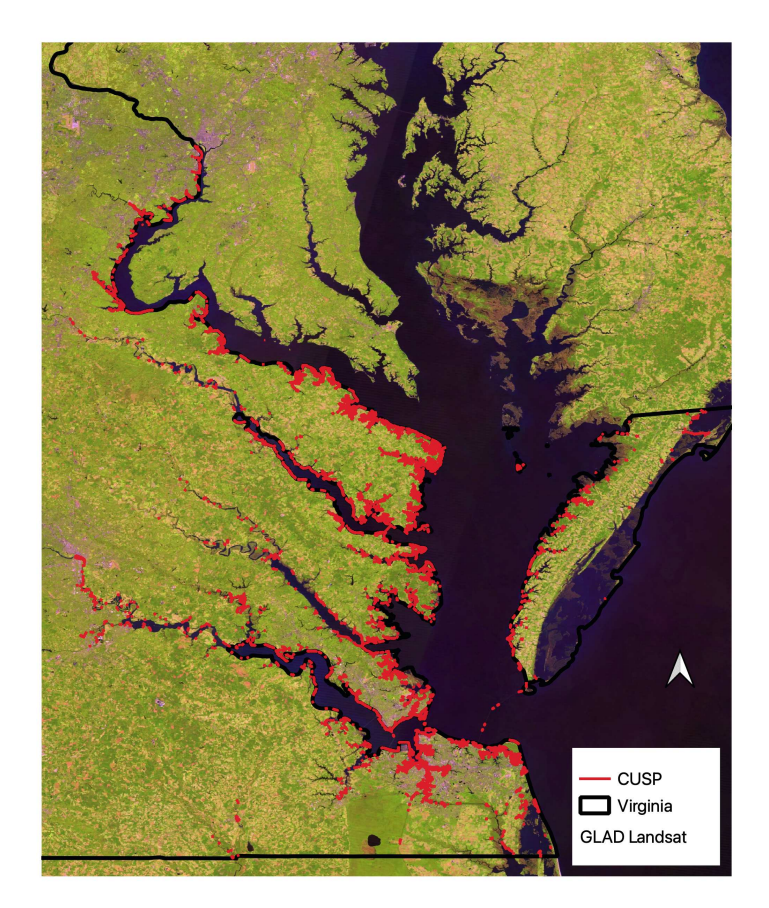


Figure 1: Shoreline structures extracted from CUSP (NOAA, 2021a) along Virginia's coastal regions (Runfola et al., 2020). Basemap is Landsat imagery downloaded from the Global Land Analysis and Discovery (GLAD, 2018).

pyShore: A deep learning toolkit for shoreline structure mapping with high-resolution orthographic imagery and convolutional neural networks

2.2. Data - Labels

148

149

150

151

152

153

174

175

176

Two different datasets are leveraged to identify the geographic location of shoreline features (i.e., to label areas as belonging to a class of shoreline structure). This information is used to train the proposed deep learning approach regarding what geometric features and colors are associated with each type of shoreline structure. The two datasets we use for labeling are the NOAA Continually Updated Shoreline Product (CUSP), and the Massachusetts Private Shoreline Stabilization Structures dataset.

2.2.1. NOAA's Continually Updated Shoreline Product

The Continually Updated Shoreline Product (CUSP) published by the National Oceanic and Atmospheric Administration (NOAA) National Geodetic Survey (NGS) provides a complete shoreline representation along the U.S. coastline and its territories (NOAA, 2021a,b). It was created to deliver accurate, contemporary shoreline information across the continental U.S to support various applications including coastal planning, hazard management and mitigation, storm management, environmental studies, and informing policy and decision makers in coastal management (NOAA, 2021b). The geographic location of shoreline along the coast of Virginia were extracted from CUSP to establish the geographic location of eligible pixels to consider for classification. It has an average line resolution of 103 meters, and covers a total of 17,239 kilometers of coastline in Virginia.

From the full coastline, we subset to 945 kilometers of shoreline at which one of four hardened shoreline structure types was identified - the focus structures of this study. These four shoreline structure types - breakwater, rip rap, groin, and bulkhead - make up the majority of shoreline structures that are built in Virginia to defend against sea level 164 rise, flooding, and coastal erosion (CCRM, 2019). Breakwater (Fig. 3d) is an always-dry (not covered at high water 165 under average meteorological conditions) structure protecting a shore area, harbor, anchorage, or basin from waves. 166 Riprap, as seen in Fig. 3c, is a shoreline structure built by layers of broken rock, cobbles, boulders, or fragments of 167 sufficient size to resist the erosive forces of flowing water and wave action. Groin (Fig. 3b) is an always-dry, shallow, 168 artificial, wall-like structure of durable material extending from the land to seaward for a particular purpose, such as 169 to prevent coast erosion. Bulkheads (or sea walls; Fig. 3a) are embankments or walls for protection against waves or 170 tidal action along a shore or waterfront. The shoreline structures metadata within CUSP was used to label pixels to its 171 corresponding shoreline structure category. Fig. 2 summarizes the number of features (i.e., discrete lines representing 172 shore features) used to label each pixel. 173

2.2.2. Massachusetts Private Shoreline Stabilization Structures

As figure 2 illustrates, the data labels from CUSP in Virginia are highly imbalanced, largely due to a limited number of labeled features for groins and breakwater. In order to increase the number of training dataset examples and create a more balanced dataset for training, we extract additional groins features from a secondary dataset published by the

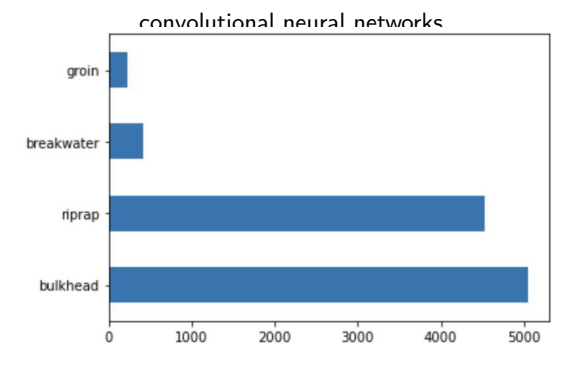


Figure 2: CUSP data distribution in Virginia.

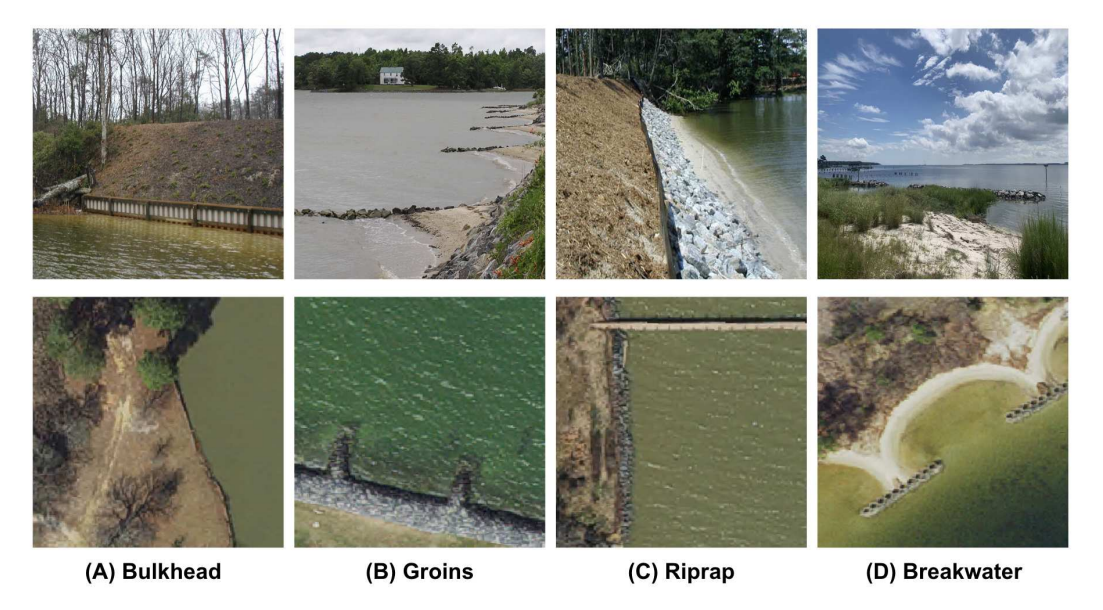


Figure 3: A visualization of the four shoreline armoring techniques we focus on in this study. The upper four images are taken on-site, and the lower four images are from VA orthoimagery

Massachusetts Coastal Infrastructure Inventory (Fontenault et al., 2013). This dataset was developed for Massachusetts
Office of Coastal Zone Management to monitor coastal structures that were built to protect public and private development in dynamic coastal areas (Fontenault et al., 2013). There are 1,957 geocoded groins available in this dataset,
collected in 2013 and digitized using 30 cm resolution 2008/2009 USGS color orthographic imagery. The digitized
groins are combined with CUSP features to construct a broader dataset for model training and validation.

2.3. Data - Imagery

185

2.3.1. Virginia Base Mapping Program (VBMP)

The Virginia Base Mapping Program (VBMP) was initiated in 2001 to develop orthoimagery for the Commonwealth of Virginia. The purpose of this program is to create a consistent, accurate base map that all state, local, and federal government agencies, as well as private sectors and academic intuitions can use for spatial data applications

(VGIN, 2018). The VBMP imagery leveraged was captured at a 12-inch (30.48cm) ground sample distance and acquired during the leaf-off period in 2021 with 3-band spectral resolution (red, green, blue) across the Commonwealth of Virginia.

We specifically leverage a total of 1,103 image tiles (the size of each image tiles varied, and the average image size is 5000×5000 pixels) that intersect with the CUSP coastal line data. Files were retrieved from VGIN in MrSID format, converted to geotiffs, and then labeled using the georeferenced CUSP data for further analysis as described above.

2.3.2. Massachusetts High-Resolution Orthoimagery

191

192

193

104

195

196

107

198

200

201

202

203

204

205

206

207

208

Thirty-centimeter resolution 2008/2009 USGS Color Ortho Imagery was retrieved for all areas covered by the Massachusetts Coastal Infrastructure Inventory Groins, representative of the same imagery used for digitization (Fontenault et al., 2013). These images are 3-band (Red, Green, Blue) natural color. A map of the bounding boxes of these images can be seen in figure 4.

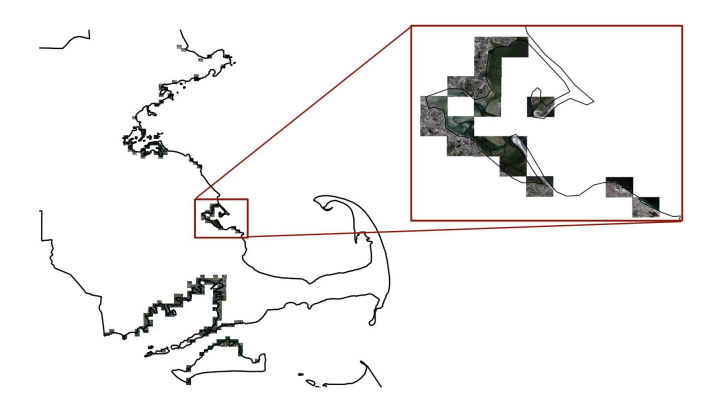


Figure 4: A map of the bounding boxes of imagery in Massachusetts with a cluster of groins near Plymouth, MA expanded. Basemap is from geoboundaries.org (Runfola et al., 2020) and imagery is from Mass.gov (USGS, 2012)

2.3.3. National Agricultural Imagery Program

Aerial images collected by the United States Department of Agriculture's (USDA) National Agricultural Imagery Program (NAIP) (OCM-Partners, 2022) were also acquired for this study in order to analyze the relationship between imagery resolution and model accuracy, as well as to explore the potential benefits of datasets incorporating a near-infrared band for shoreline structure identification.

The NAIP dataset is a time series aerial imagery database that has records extending to 2003, sponsored through a collaboration between the United States Geological Survey (USGS) and U.S. state governments (OCM-Partners, 2022). The initial NAIP acquisition cycle was five years, before changing to three years in 2009. NAIP imagery is generally acquired at a 1-meter spatial resolution with 4-band spectral resolution (red, green, blue and near-infrared) across the continental United States during the agricultural growing season. In recent years, some states began publishing the

dataset with higher spatial resolution (including Virginia). Imagery is provided orthorectified; for our study, we use the NAIP imagery acquired 2018 in Virginia with 0.6 m spatial resolution. A total of 316 image tiles (standardized to a size of 5000 × 5000 pixels) provided complete coverage of all coastal features in the CUSP database.

2.4. Data processing - annotation process & protocol

210

211

216

217

218

219

220

221

222

223

224

225

226

A python processing script was developed to automate data pre-processing, labelling, and generation of training and validation data. Of the 10,194 filtered shoreline structures identified in CUSP coastal lines (1,055 km), 5,040 (529 km) were labeled bulkhead, 4,519 (489 km) riprap, 221 (6 km) groin, and 414 (31 km) breakwater. A 3-meter buffer was constructed along the filtered shoreline structures in order to provide context for image classification as well as mitigate minor errors or differences in georeferencing across imagery and shoreline label sources.

Here we present a brief example of our processing procedures, using NAIP imagery as an illustrative case. First, each 5000×5000 pixel NAIP image tile is cropped into 400 256×256 image patches. Only image patches that intersect with CUSP features are kept for further data processing and analysis, resulting in a dataset of 4,532 256 × 256 tiles covering coastal Virginia. The pixels in these image patches are labeled using the CUSP dataset, by first masking all pixels that are not shoreline as background, and then labeling the remaining pixels according to the corresponding class values in CUSP (bulkhead, riprap, groin, and breakwater). This procedure results in a series of 256 × 256 masks with each shoreline pixel labelled. Fig. 5 is an example of an original NAIP tile, cropped to 256 × 256 pixels, and the corresponding label mask on the right. This data is used to construct training, validation, and testing datasets for the model development, calibration, and validation.

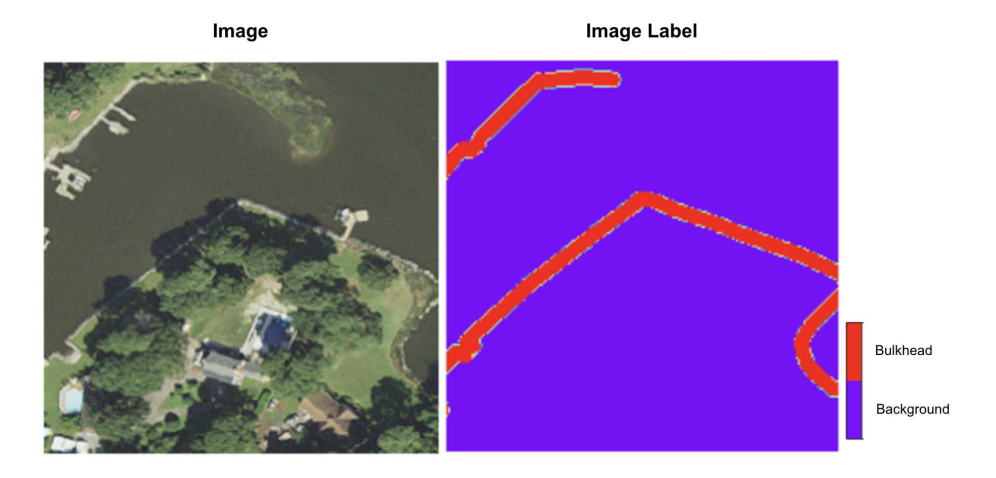


Figure 5: An example case of cropped image patch and its associated mask.

In addition, for each 256×256 tile, a secondary dataset is generated in which the entire image is labeled as a single class based on the most common shoreline structure. This secondary dataset is used to establish baseline accuracy of

pyShore: A deep learning toolkit for shoreline structure mapping with high-resolution orthographic imagery and convolutional neural networks

Table 1

Summary of the number of pixels (and percentage) in each dataset used in model training and testing. The green column represents number of pixels labeled as bulkhead, the red column represents number of pixels labeled as riprap, the yellow column indicates the number of pixels labeled as groin, and the blue column shows the number of pixels labeled as breakwater.

Dataset Name	(pixel co		ng Data ercentag	e per class)	Testing Data (pixel count and percentage per class)						
VA CUSP/VBMP	1806539	1704174	91117	214871	391008	330605	23377	50356			
VA COSF/VBIVIE	47%	45%	2%	6%	49%	42%	3%	6%			
VA CUSP/VBMP & MA	1806539	1704174	374952	214871	406597	427725	270849	81867			
VA COSF/VBIVIF & IVIA	44%	42%	9%	5%	29%	24%	43%	4%			
VA CUSP/NAIP	2727071	2660187	60866	242668	599562	536705	14662	54891			
VA COSP/NAIP	48%	47%	1%	4%	50%	46%	1%	6%			

methodologies that do not involve localization (i.e., to contrast pixel vs. scene resolution classification accuracy).

This process is repeated for three datasets - VBAP images, MA high-resolution orthoimagery, and NAIP. We leveraged these datasets to conduct a wide range of tests regarding the performance of our approach under a range of different circumstances.

Of the collected shoreline structure images and labels in the three datasets, the number of pixels per each class in the training and testing subsets are summarized in Table 1. Observed data imbalance is taken into account in the training process with a weighting scheme on the loss function; we present details of our approach in section 2.5.

2.5. Methodology

233

234

235

236

237

2.5.1. Architectures for image segmentation

Three predefined state-of-the-art semantic segmentation architectures are tested and compared considering their generalization capacities, U-Net (Ronneberger et al., 2015), DeeplabV3 (Chen et al., 2016), as well as Pyramid Attention Network (PAN) (Li et al., 2018).

U-Net: The U-Net is a well-established, relatively light weight (under 10 million parameters and forward-pass timings of less than a second for 256 × 256 images) deep learning algorithm for semantic segmentation based on convolutional network architectures (Ronneberger et al., 2015). The algorithm's architecture includes two parts: downsampling and up-sampling, also called the encoder and decoder. The encoder extracts varying resolution feature maps through a series of convolutional, rectified linear units (ReLU), and max-pooling layers (Li et al., 2021). The decoder stage contains and combines (a) each feature map from the down-sampling process, and (b) spatial information through an up-sampling and concatenation process (Fig. 6). This data flow of down-sampling and up-sampling constructs a U-shape of architecture, thus the output layer maintains the same resolution as the input layers. One key benefit of using this learning architecture is that it has been shown to be effective in cases with few training images, while still

retaining high levels of segmentation accuracy (Ronneberger et al., 2015).

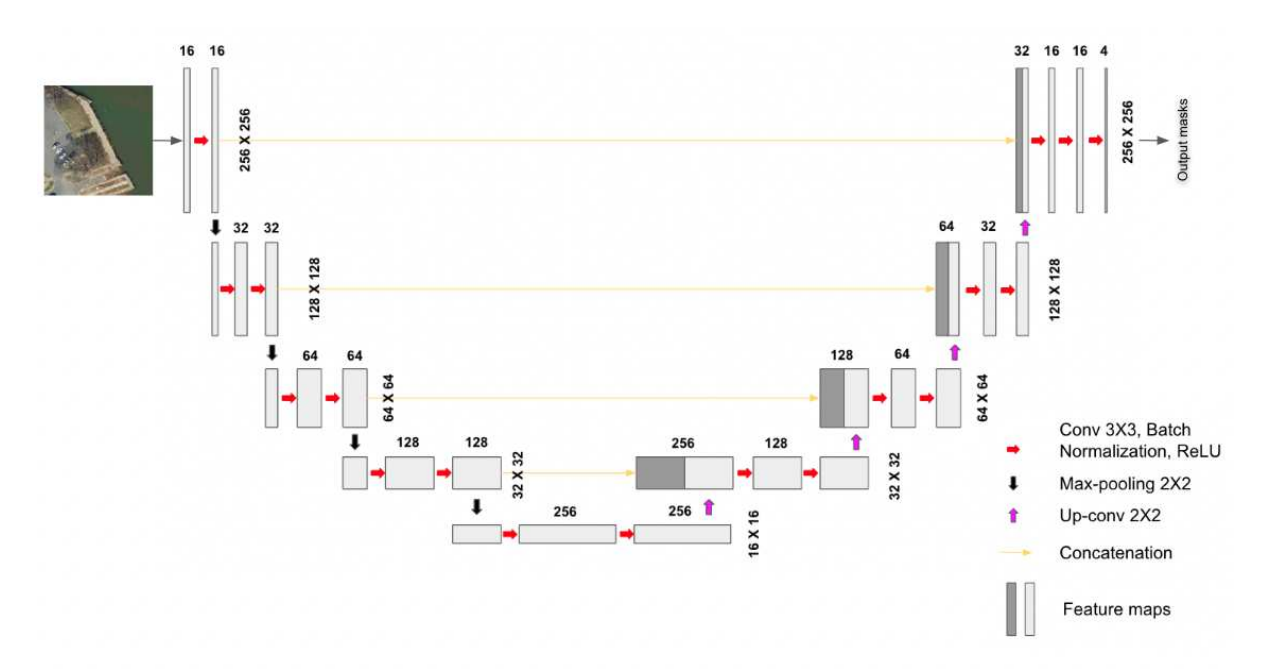


Figure 6: The U-Net architecture (Example of a 3-band input image with 256×256 pixel-size). The boxes indicate the feature maps at each layer, and the number on the top of each feature map shows the depth of feature map (channel). Numbers on the right side of each feature map are image/feature maps dimension.

In this piece, we modify the U-Net architecture in order to identify a deep learning model that can both accurately delineate shoreline structures, and do so in a way that is computationally suitable for deployment on contemporary desktops and laptops. We modify the U-Net in two key ways: (a) we provision alternative classifiers to handle encoding and decoding tasks, and (b) we adapt the algorithm to dynamically accept either 4-band (RGB,NIR) or 3-band (RGB) high-resolution imagery (noting our labeled data is sourced from both three and four band sensors). The specific alternative classifiers that are contrasted in this piece to assess their capabilities in shoreline structure detection include modifications to the U-Net which leverage a small set of convolutional approaches chosen for their relative computational efficiency - Resnet-18, Xception, and the original U-Net implementation (Ronneberger et al., 2015) - as well as two deeper (i.e., more computationally intensive) networks to provide contrasting cases - Resnet-101 and InceptionResNet-v2.

DeeplabV3: The DeeplabV3 algorithm is designed for image segmentation. It introduces atrous convolution (Chen et al., 2016) in the down-sampling process to efficiently produce high level feature maps while keeping accurate location information, which can effectively enlarge the field of view of filters without increasing the number of training parameters. The deeplabV3 also uses atrous spatial pyramid pooling (ASPP) to capture objects and useful image context at multiple scales (Chen et al., 2016). This method has recently been applied in many semantic segmentation tasks

251

258

259

260

261

262

263

264

convolutional neural networks

with remote sensing data and proved to be an effective technique in many fields (Wang et al., 2022; Liu et al., 2021).

Pyramid Attention Network: Different from U-Net and DeeplabV3, PAN is built on an attention mechanism, which
 aims to imitate human visual systems to effectively find salient regions in a complex scene. The attention mechanism
 is combined with spatial pyramid to extract precise dense features for pixel labeling (Li et al., 2018), instead of using
 atrous convolution like DeeplabV3 and artificially designed decoder networks like U-Net.

Within each of these architectures, we further test a range of up- and down-sampling convolutional strategies, including Resnet-18, Resnet-101, xception, and InceptionResnet.

2.5.2. Loss functions

The loss function is the proximity between the ground truth label data and the predicted class. In this study, we implement a multi-class cross-entropy loss:

$$loss = -\sum_{c=1}^{M} y_{o,c} \log(p_{o,c})$$
 (1)

where M is the total number of shoreline structure classes (M = 4 in this study, background is excluded from the loss)
and y is the binary indicator (0 or 1) if class label c is the correct classification for observation o, p is the predicted
probability observation o is of class c. Due to the imbalance of our pixel-level data distribution, a weighting scheme is
used in the training process, in which classes are weighed according to their representation in the labeled data (Kikaki
et al., 2022; Paszke et al., 2016):

$$W_{class} = \frac{1}{\ln(c + p_{class})} \tag{2}$$

where W_{class} is a multiplicative weight applied to the loss function for observations of a given class, $p_{class} = N_{pixelsof class}$ / $N_{totalpixels}$, where $N_{totalpixels}$ excludes the background pixels in the training set, and c is an additional hyper-parameter set to 1.03 (following past literature; see Kikaki et al. (2022)). During the training process, Adam optimization is used to minimize the cross-entropy loss with an initial learning rate of 1×10^{-3} .

2.5.3. Model validation and application

We implement a wide range of validation metrics to assess pixel-level semantic segmentation performance. First and foremost, we present overall accuracy (equation 3) to give guidance to the overall performance a user might expect.

In addition, we evaluate the intersection-over-union (IoU) (equation 4), the average F1 score for each class (Macro-F1)

convolutional neural networks

(equation 5), and the precision (equation 6) and recall (equation 7) at the pixel level for each class.

$$Accuracy = \frac{TP + TN}{TP + TN + FP + FN}$$
(3)

$$IoU(U, V) = \frac{|U \cap V|}{|U \cup V|} \tag{4}$$

$$F1 = \frac{2 * Precision * Recall}{Precision + Recall} = \frac{2 * TP}{2 * TP + FP + FN}$$
(5)

$$Precision = \frac{TP}{TP + FP} \tag{6}$$

$$Recall = \frac{TP}{TP + FN} \tag{7}$$

In equations 3, 5, 6, and 7, TP (true positive) represents the number of pixels in which the model correctly predicts ground truth, TN (true negative) represents outcomes in which the model correctly predicts cases that are different than ground truth, FP (false positive) is predictions to a class that do actually not belong to that class, and FN (false negative) are the number of predictions belonging to a class but were predicted to be in a different class. The F1 score is a harmonic mean between precision and recall.

The IoU (equation 4), defined as the size of the intersection divided by the size of the union of two label sets, is used to compare the set of predictions for a sample to the corresponding set of ground truth labels. IoU provides a conservative estimate of model performance, penalizing for both FP and FN at the pixel level (Rezatofighi et al., 2019).

Lastly, a cross-validation matrix for each model is additionally generated to compare the prediction accuracy for each

type of shoreline structure.

3. Results & Analysis

310

311

312

313

328

The results of each test, including permutations of the datasets described in section 2.3 and the architectures described in section 2.5.1, are presented in Table 2; the results for tests using NAIP imagery are summarized in Table 3.3.

The first set of results (the first three rows) in Table 2 present a U-Net implementation in which the encoder and decoder is the same as in the original definition of the architecture (Ronneberger et al., 2015) (i.e., a "Backbone" of "Original"). In Table 2, in order to evaluate model performance in the Virginia region specifically, we delineate between models that are tested solely on coastal features in Virginia, and those that are tested on a dataset which includes both Virginia and Massachusetts features. For example, the results indicate that when the "Original" U-Net implementation is tested (with the default encoder and decoder):

- 1. When trained and tested on the integrated Virginia and Massachusetts (VA and MA) datasets, the overall accuracy (OA) is 75%; the best performing class is Groins (F1 = 0.96); worst is Breakwater (F1 = 0.4).
- 2. When trained on VA and MA, but then tested only on VA, the overall accuracy is 59%.
- 3. When trained on VA data alone, and then tested on VA alone, the overall accuracy is 61%.

Thus, the first set of our results provides evidence that suggests that - if a default U-Net implementation is leveraged the best overall model performance across all of our data is found if all data from VA and MA is pooled. However, for
the model we are most interested in - a model that succeeds in classifying the Chesapeake Bay and related shorelines
in Virginia - we find that limiting training data to Virginia can result in a slightly better performing model based on
overall accuracy.

We expand this study to a range of alternative classifiers ("backbones"), in which we exchange the default encoder and decoder of the U-Net, DeeplabV3, PAN architecture with a range of popular network architectures (Resnet-18 and Resnet-101 for all three architectures, xception and inceptionResnetV2 for U-Net, with transfer learning weights based on ImageNet). Across all of these permutations, we identify PAN-resnet101 as the best global classifiers, achieving 83% overall accuracy when trained and tested on the integrated Virginia and Massachusetts dataset. The performance of PAN-resnet18 is particularly notable in this scenario, as it achieved 81% overall accuracy, but with far less complexity (11M parameters) than the best classifier (43M). This indicates that a lighter-weight architecture may be appropriate for shoreline structure delineation, which can enable deployment on - for example - lower memory environments.

When focusing only on validation with Virginia basemap (3-band) imagery data, we find the highest overall validation accuracy is 72% (using PAN-resnet101 implementations). Using the lighter weight PAN-resnet18, the overall validation accuracy achieved was 69%. Similar to the joint Massachusetts and Virginia case, this highlights the value

Table 2Results of Architecture Tests. Results are presented broken out by model implementation, test and training datasets, and each of the four tested classes. Each tested class is presented

with four statistics: F1 score (F1), Intersection over Union (IoU), Precision (Prec.), and Recall (Rec.). Global statistics are presented in the final four columns, including mean Intersection over Union (mIOU), Overall Accuracy (OA), and Macro-Averaged F1 score (F1-macro).

Mod	lel Details	Datase	t Name		Bull	chead			Rip	orap			Gr	oins			Break	water		mIOU	OA	F1-macro
Architecture	Decoder	Trained	Tested	F1	IOU	Prec.	Rec.	F1	IOU	Prec.	Rec.	F1	IOU	Prec.	Rec.	F1	IOU	Prec.	Rec.	miou	UA	F1-IIIaCro
	Original	VA&MA	VA&MA	0.66	0.5	0.68	0.65	0.54	0.37	0.55	0.53	0.96	0.93	0.99	0.94	0.4	0.25	0.29	0.6	0.51	0.75	0.64
UNet	param: 0.8M	VA&MA	VA	0.67	0.5	0.68	0.65	0.55	0.38	0.57	0.53	0.27	0.16	0.42	0.2	0.41	0.26	0.31	0.6	0.32	0.59	0.47
	param: 0.0ivi	VA	VA	0.67	0.51	0.71	0.64	0.59	0.42	0.57	0.6	0.28	0.16	0.4	0.21	0.42	0.26	0.34	0.54	0.34	0.61	0.49
	Resnet-18	VA&MA	VA&MA	0.68	0.52	0.71	0.65	0.61	0.44	0.59	0.63	0.96	0.93	0.96	0.97	0.55	0.38	0.52	0.58	0.57	0.78	0.7
UNet	14.3M	VA&MA	VA	0.68	0.52	0.71	0.65	0.61	0.44	0.6	0.63	0.35	0.21	0.3	0.41	0.56	0.39	0.53	0.58	0.39	0.63	0.55
	14.3IVI	VA	VA	0.73	0.57	0.73	0.72	0.64	0.47	0.63	0.65	0.41	0.25	0.73	0.28	0.52	0.35	0.47	0.59	0.41	0.67	0.57
	Resnet-101	VA&MA	VA&MA	0.72	0.56	0.74	0.69	0.66	0.49	0.62	0.69	0.97	0.94	0.97	0.96	0.56	0.39	0.59	0.54	0.59	0.8	0.73
UNet	51.5M	VA&MA	VA	0.72	0.56	0.75	0.69	0.66	0.49	0.63	0.69	0.41	0.26	0.4	0.42	0.57	0.4	0.61	0.54	0.43	0.68	0.59
	31.31/1	VA	VA	0.75	0.6	0.75	0.75	0.68	0.51	0.67	0.68	0.53	0.36	0.68	0.44	0.6	0.43	0.57	0.64	0.48	0.71	0.64
	xception	VA&MA	VA&MA	0.73	0.58	0.78	0.69	0.69	0.53	0.63	0.77	0.98	0.96	0.99	0.97	0.58	0.41	0.69	0.5	0.62	0.82	0.75
UNet	UNet 29M	VA&MA	VA	0.73	0.58	0.79	0.69	0.69	0.53	0.63	0.77	0.55	0.38	0.64	0.49	0.59	0.42	0.71	0.5	0.48	0.7	0.64
	29W	VA	VA	0.77	0.62	0.76	0.77	0.7	0.54	0.69	0.7	0.47	0.31	0.43	0.52	0.6	0.43	0.7	0.53	0.47	0.72	0.63
	inceptionresnetv2	VA&MA	VA&MA	0.74	0.58	0.76	0.71	0.68	0.52	0.64	0.73	0.98	0.96	0.99	0.97	0.59	0.42	0.67	0.52	0.62	0.82	0.75
UNet	JNet 62M	VA&MA	VA	0.74	0.58	0.77	0.71	0.69	0.52	0.65	0.73	0.58	0.41	0.63	0.53	0.59	0.42	0.69	0.52	0.48	0.7	0.65
	UZIVI	VA	VA	0.75	0.6	0.76	0.73	0.69	0.52	0.66	0.72	0.53	0.36	0.74	0.42	0.51	0.34	0.52	0.5	0.46	0.7	0.62
	Resnet-18	VA&MA	VA&MA	0.66	0.49	0.7	0.62	0.58	0.41	0.55	0.62	0.95	0.9	0.95	0.94	0.48	0.31	0.44	0.53	0.53	0.76	0.67
DeeplabV3	16M	VA&MA	VA	0.66	0.49	0.7	0.62	0.59	0.42	0.56	0.62	0.41	0.26	0.32	0.56	0.54	0.37	0.56	0.53	0.38	0.61	0.55
	TOIVI	VA	VA	0.68	0.52	0.7	0.67	0.61	0.44	0.59	0.63	0.36	0.22	0.42	0.31	0.56	0.39	0.59	0.53	0.39	0.64	0.55
	Resnet-101	VA&MA	VA&MA	0.7	0.54	0.72	0.68	0.61	0.44	0.59	0.63	0.95	0.91	0.96	0.94	0.46	0.3	0.41	0.53	0.55	0.78	0.68
DeeplabV3	59M	VA&MA	VA	0.7	0.54	0.73	0.68	0.62	0.45	0.61	0.63	0.36	0.22	0.32	0.41	0.51	0.34	0.49	0.53	0.39	0.64	0.55
	39W	VA	VA	0.74	0.58	0.76	0.72	0.67	0.51	0.64	0.7	0.49	0.33	0.53	0.46	0.52	0.35	0.55	0.5	0.44	0.69	0.61
	Decret 10	VA&MA	VA&MA	0.74	0.58	0.72	0.75	0.65	0.48	0.65	0.65	0.97	0.94	0.97	0.96	0.6	0.43	0.66	0.55	0.61	0.81	0.74
PAN	PAN Resnet-18	VA&MA	VA	0.74	0.58	0.73	0.75	0.65	0.48	0.65	0.65	0.47	0.31	0.45	0.5	0.64	0.48	0.78	0.55	0.46	0.69	0.63
	TIM	VA	VA	0.73	0.57	0.72	0.74	0.66	0.49	0.65	0.67	0.52	0.35	0.83	0.38	0.7	0.54	0.83	0.6	0.49	0.69	0.65
	Resnet-101	VA&MA	VA&MA	0.76	0.61	0.76	0.75	0.69	0.53	0.69	0.7	0.98	0.95	0.99	0.97	0.63	0.46	0.57	0.7	0.64	0.83	0.76
PAN	43M	VA&MA	VA	0.76	0.61	0.76	0.75	0.69	0.53	0.69	0.7	0.51	0.34	0.56	0.46	0.65	0.48	0.61	0.7	0.49	0.72	0.65
	43IVI	VA	VA	0.75	0.6	0.75	0.76	0.68	0.51	0.66	0.7	0.51	0.34	0.79	0.37	0.56	0.39	0.66	0.49	0.46	0.7	0.63

of the lighter weight PAN-resnet18 implementation; further, we note that UNet-xception came in a close second with 70% accuracy (29M parameters).

In the results presented in Table 2, the models trained on the Virginia dataset have no particular class correlated closely with overall performance. The overall accuracy in Virginia shoreline features ranges from 61% to 72%, with each model performing relatively poorly with groins (noting model performance varies most in this class). With 391,008 pixels labeled as bulkhead in the Virginia test set, each model performed relatively well at prediction of the class, with relatively little variance (0.05%) across models.

Introducing additional examples of groin features into the training dataset proved to be relatively inefficient in improving overall accuracy for the Virginia data, suggesting that groin features in Massachusetts and those in Virginia may be distinct enough to require specialized approaches to cross-domain learning. However, for model development that may be focusing on global results (i.e., not domain specific to Virginia), the additional samples had a range of advantages. Adding the geocoded groin features from MA into training, the precision for predicting groins improved dramatically - for UNet-xception tested on VA to the same model tested on the merged MA and VA dataset - from 43% to 99%. For groin features specifically, the best model tested on the merged dataset achieves 99% accuracy, 97% recall, and 98% F1 score. Figure 7 presents the visualization of predictions from models trained on Virginia VBMP dataset.

Table 3 highlights results when models are tested using only Virginia imagery (testing and training) with the NAIP dataset. We find broadly comparable results to the cases presented in Table 2, with a slight performance gain in the

330

331

332

333

334

335

336

337

338

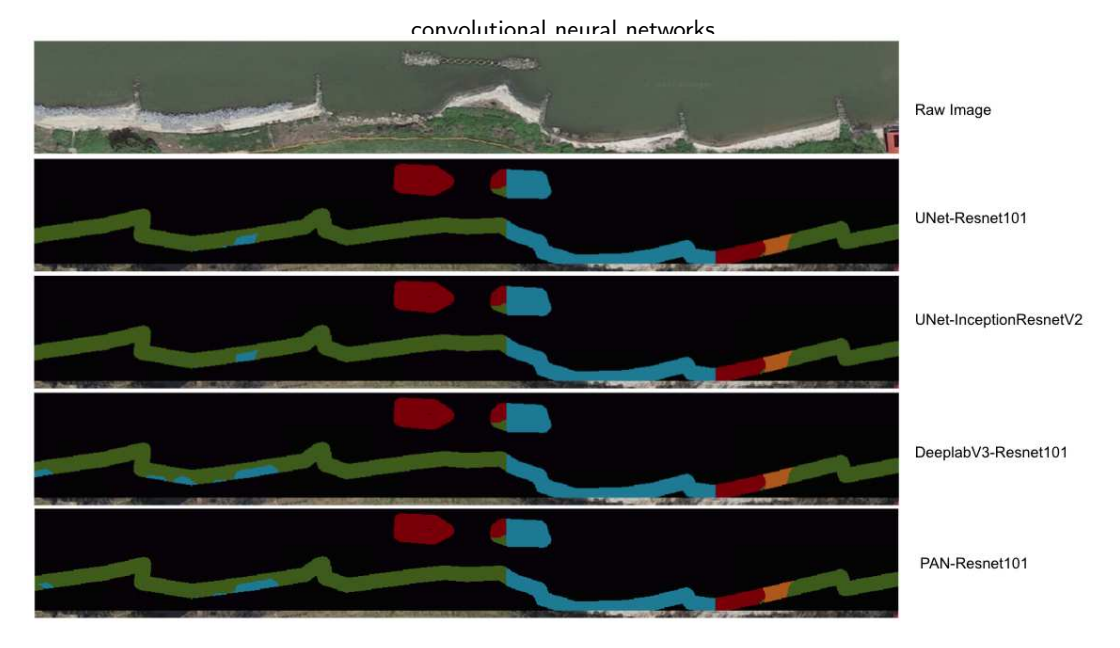


Figure 7: Result visualization predicted by different models trained on VBMP 3-band imagery.

Table 3Architecture results with NAIP imagery. Each tested class is presented with four statistics: F1 score (F1), Intersection over Union (IoU), Precision (Prec.), and Recall (Rec.). Global statistics are presented in the final four columns, including mean Intersection over Union (mIoU), Overall Accuracy (OA), and Macro-Averaged F1 score (F1-macro).

Mod	Model Details Dataset Name			Bulkhead			Riprap				Groins				Breakwater				mIOU	OA	F1-macro	
Architecture	Decoder	Trained	Tested	F1	IOU	Prec.	Rec.	F1	IOU	Prec.	Rec.	F1	IOU	Prec.	Rec.	F1	IOU	Prec.	Rec.	50	UA	1 I-macro
UNet	Original params: 0.8M	VA	VA	0.7	0.54	0.73	0.68	0.65	0.5	0.67	0.67	0.4	0.29	0.38	0.55	0.65	0.48	0.53	0.84	0.45	0.68	0.62
UNet	Resnet-18 14.3M	VA	VA	0.73	0.57	0.72	0.74	0.67	0.51	0.67	0.67	0.54	0.37	0.76	0.42	0.7	0.54	0.79	0.63	0.5	0.7	0.66
UNet	Resnet-101 51.5M	VA	VA	0.73	0.58	0.73	0.74	0.68	0.51	0.68	0.68	0.58	0.41	0.67	0.51	0.71	0.56	0.75	0.68	0.51	0.71	0.68
UNet	Xception 29M	VA	VA	0.74	0.58	0.72	0.76	0.68	0.51	0.69	0.67	0.6	0.43	0.76	0.5	0.74	0.58	0.85	0.65	0.53	0.71	0.69
UNet	InceptionResnetV2 62M	VA	VA	0.76	0.62	0.74	0.79	0.71	0.55	0.73	0.69	0.68	0.52	0.77	0.61	0.75	0.6	0.85	0.68	0.57	0.72	0.73
DeeplabV3	Resnet-18 16M	VA	VA	0.72	0.56	0.7	0.74	0.66	0.49	0.67	0.64	0.57	0.4	0.67	0.5	0.68	0.51	0.72	0.64	0.49	0.69	0.66
DeeplabV3	Resnet-101 59M	VA	VA	0.73	0.58	0.72	0.74	0.68	0.52	0.69	0.67	0.49	0.32	0.48	0.5	0.66	0.49	0.67	0.65	0.48	0.7	0.64
PAN	Resnet-18 11M	VA	VA	0.75	0.6	0.71	0.8	0.68	0.51	0.72	0.64	0.55	0.38	0.94	0.39	0.76	0.61	0.8	0.72	0.53	0.72	0.69
PAN	Resnet-101 43M	VA	VA	0.75	0.6	0.72	0.78	0.68	0.5	0.7	0.67	0.54	0.37	0.86	0.4	0.67	0.5	0.79	0.57	0.5	0.71	0.66

best overall accuracy at 74% (UNet-inceptionResnetV2, 62 million parameters). Each model performs relatively well
at predicting bulkhead and riprap features, with significantly less variance between the models than observed in the
models trained and validated based on the Virginia basemap and Massachusetts 3-band orthoimagery. Of note is that
the PAN-Resnet18 model achieves 94% and 80% precision in groins and breakwater, despite the relatively small number
of labeled cases available (see Fig.2). Fig. 8 summarizes the precision improvement for each class when contrasting
models fit in Virginia using the VBMP orthoimagery and NAIP imagery.

To better understand the contribution of the NIR band in NAIP imagery to model performance compared to using only RGB orthoimagery, we further trained each model with 3-band (RGB) NAIP imagery - excluding the fourth

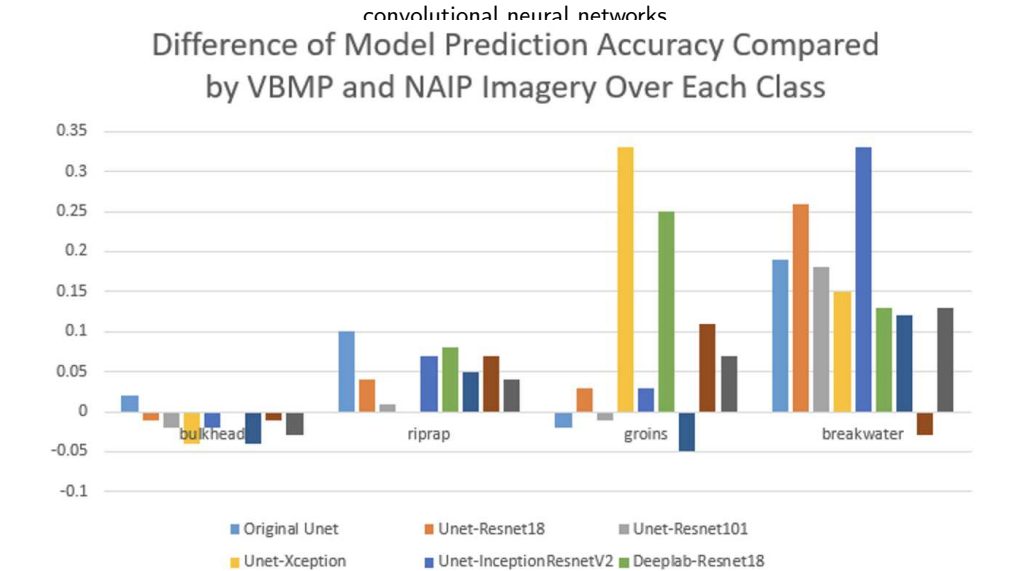


Figure 8: Performance comparison between models trained on VBMP and NAIP

■ Deeplab-Resnet101

The values in this chart are calculated by subtracting the model prediction accuracy of each class trained on VBMP imagery from the prediction accuracy trained on NAIP imagery. Positive values correspond to improvement after using NAIP imagery.

■ PAN-Resnet18

■ PAN-Respet101

Table 4
Model performance using 3-band NAIP imagery (excluding near infrared).

Mod	Model Details Dataset Name			Bulkhead				Riprap				Groins				Breakwater				mIOU	OA	Fa-macro
Architecture	Decoder	Trained	Tested	F1	IOU	Prec.	Rec.	F1	IOU	Prec.	Rec.	F1	IOU	Prec.	Rec.	F1	IOU	Prec.	Rec.	IIIIOO	UA	Fa-IIIaCro
UNet	Resnet-18	RGB	RGB	0.7	0.54	0.71	0.7	0.66	0.49	0.64	0.67	0.59	0.42	0.83	0.46	0.69	0.53	0.79	0.61	0.5	0.68	0.66
UNet	Resnet-101	RGB	RGB	0.72	0.56	0.7	0.73	0.66	0.5	0.67	0.66	0.48	0.31	0.63	0.38	0.65	0.48	0.75	0.58	0.46	0.69	0.63
UNet	Xception	RGB	RGB	0.74	0.59	0.72	0.76	0.69	0.52	0.7	0.68	0.62	0.45	0.86	0.48	0.75	0.6	0.86	0.67	0.54	0.72	0.7
UNet	InceptionResnetV2	RGB	RGB	0.76	0.61	0.74	0.77	0.71	0.55	0.71	0.71	0.7	0.53	0.87	0.58	0.73	0.57	0.85	0.64	0.57	0.72	0.72
DeeplabV3	Resnet-18	RGB	RGB	0.71	0.55	0.69	0.73	0.64	0.47	0.65	0.63	0.53	0.36	0.65	0.45	0.68	0.52	0.75	0.63	0.47	0.67	0.64
DeeplabV3	Resnet-101	RGB	RGB	0.74	0.59	0.73	0.76	0.69	0.52	0.7	0.68	0.54	0.37	0.63	0.48	0.68	0.51	0.74	0.62	0.5	0.71	0.66
PAN	Resnet-18	RGB	RGB	0.74	0.59	0.71	0.78	0.67	0.51	0.71	0.64	0.6	0.43	0.89	0.45	0.74	0.59	0.81	0.69	0.53	0.71	0.69
PAN	Resnet-101	RGB	RGB	0.73	0.58	0.73	0.73	0.68	0.52	0.68	0.68	0.54	0.37	0.69	0.45	0.67	0.5	0.69	0.65	0.49	0.71	0.66

infrared band (see table 4). Compared to table 3, overall accuracy varied by 1% to 2%, depending on the model. Models with complex structures such as UNet-xception and DeeplabV3-Resnet101 tended to have a decrease in accuracy. The change in model performance for each architecture varies, with a small decrease in precision on groins in the more complex model architecture. However, when using PAN-resnet18, the prediction accuracy on groins increased to 94%.

4. Discussion

360

361

362

363

The overall results of this study illustrate that, leveraging NAIP 4-band NIR imagery, classification accuracy of bulkhead, riprap, groins and breakwater shoreline structures can reach approximately 74% in the Virginia study area; accuracy of up to 83% was observed in the models pooling Virginia and Massachussets shoreline structure data. Notably, this accuracy is a pixel-level metric - i.e., the number of approximately 60 centimeter pixels that are classified correctly. While higher levels of accuracy may be required for a fully automated approach, by integrating this into

a semi-automated pipeline in which first the presented algorithm is applied, and second a human coder corrects the output, significant time savings can be gained as contrasted to the multiple-year process currently being used by state and federal agencies. In this section, we explore model performance, highlight a number of directions for future research, and introduce a new ArcGIS python based toolkit that enables practitioners to leverage these algorithms in a semi-automated fashion.

4.1. Feature Detection

384

385

386

387

388

One frequent criticism of deep learning models is their black-box approach to image recognition, in which it can be difficult to ascertain why the model is performing (or failing) at a given task. To explore the mechanisms driving the 372 presented models, we apply a SHAP visualization (SHapley Additive exPlanations visualization technique (Lundberg 373 and Lee, 2017)) to understand what factors contribute to the model's capability to distinguish different shoreline fea-374 tures. Figure 9 shows an example of what factors played into the correct classification of two images in the ResNet-18 375 based network. In Figure 9A, an example of riprap is shown in the first row, and to the right are the features that were 376 important for a given classification - i.e., the correct classification (riprap) was due to features shown in red on the im-377 age map. As this image shows, the algorithm leverages feature information spatially proximate to the class of interest. 378 Conversely, the final column of Figure 9A also shows that indicators of riprap contribute negatively to classifications 379 of groins - i.e., the algorithm can clearly distinguish between riprap and groin features. A more complex example 380 is shown in Figure 9B, in which the true class (breakwater) is identified, but the information used for distinguishing 381 between breakwater and groin is more diffuse - i.e., contextual information is being leveraged, rather than only pixels 382 explicitly containing the breakwater feature. 383

4.2. Computational Efficiency as a product of Imagery Source & Bands

Our findings suggest that relatively less complex networks are some of the strongest performers for the task of shoreline feature detection. This is shown by the strong performance of PAN-Resnet18 in the NAIP tests, providing one of the highest levels of accuracy 72% in the Virginia case despite having one of the lowest number (11 million) of parameters to fit. While the other network architectures were able to achieve similar levels of accuracy in the context of a fourth band (UNet-InceptionResnetV2 achieved 72% accuracy), it does so with more model overhead (62 million parameters). This suggests that PAN-Resnet18 based implementations provide a strong balance between accuracy and computational costs for end-user deployment.

However, if the user only has 3-band information available to them, UNet-xception may provide the best combination of accuracy and complexity - providing similar levels of accuracy (82% in the MA/VA joint case) at a much lower parameter count than the similarly performing UNet-inceptionresnetV2 (29M vs. 62M in UNet-InceptionresnetV2). In terms of practical implementation, we find that our fully fit PAN-resnet18 model can be deployed with a memory

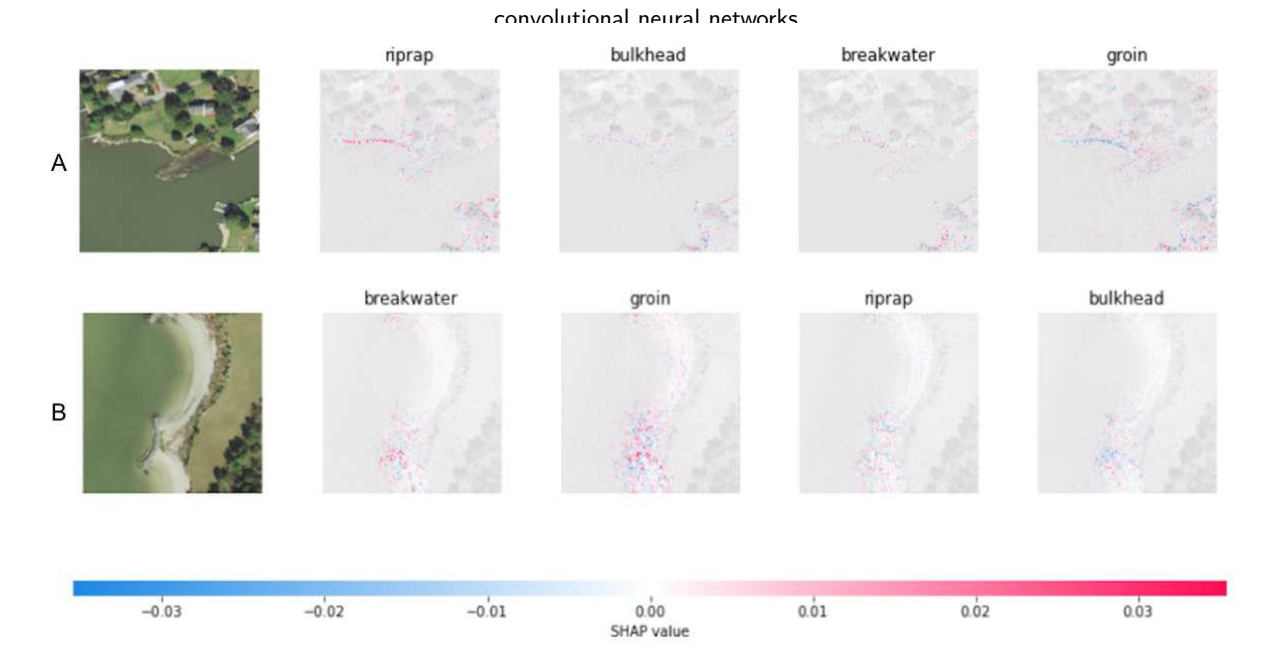


Figure 9: Virginia shoreline structure prediction analysis.

The above shows two random correctly classified test images in the first column. The second, third, fourth, and fifth columns show the pixels/features that contributed against and in favor of prediction for each of the four classes. For example, the upper-left image is a riprap structure that was predicted by the model most likely to be a riprap, then bulkhead, breakwater, and groin. Blue pixels represent areas that work against classification in a given class and the red pixels represent areas that work for classification. In this case, the Resnet-18 based network for image classification was investigated.

footprint of only 43.4 megabytes, and an estimate for 1.5 kilometers of shoreline can be generated in between 1.4 seconds (GPU) and 2.16 seconds (CPU), indicating it is suitable for general use in desktop environments. For users that
do not have a near-infrared band available, the UNet-xception implementation requires 110 megabytes of memory to
load, and can generate estimates for 1.5 kilometers of shoreline in between 2 seconds (GPU) and 9.52 seconds (CPU),
see Table 5 for computational time tested using 3-band VBMP imagery. This highlights the importance of identifying
the fourth band of information to enhance efficiency, but we also note that both models are reasonable to consider for
deployment relative to the decades-long time periods fully manual workflows require.

4.3. Difference in Shoreline Structure Data Sources

When comparing groin structures from the VA CUSP and MA data, we find that the features in MA are consistently labeled as perpendicular to the shoreline; this contrasts to the CUSP data, in which many groin features are coded along the shoreline and difficult to distinguish from other structures by eye (see Figure 10). Additionally, we found that digitization in the VA dataset is frequently not fully aligned with the structures visible in imagery (see Figure 11). These differences result in a number of limitations - and future directions - for this study. Because the Virginia data

403

404

405

406

Table 5A summary of computational time when making the 5 km prediction with 3-band VBMP imagery

Model Name	Computational Time (seconds)
UNet-Resnet18	5.27
UNet-Resnet101	13.07
UNet-xception	9.52
UNet-InceptionResnetV2	15.12
DeeplabV3-Resnet18	11.59
DeeplabV3-Resnet101	36.89
PAN-Resnet18	3.66
PAN-Resnet101	11.27

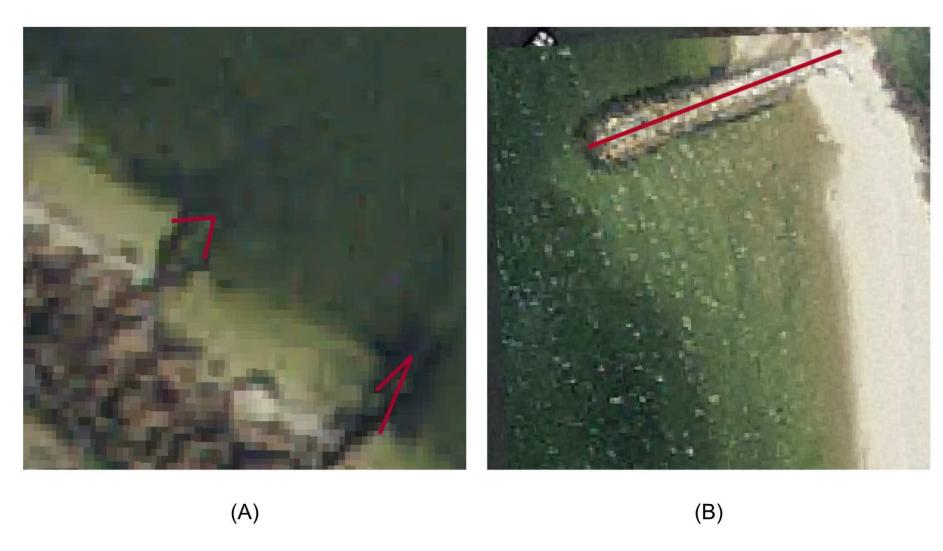


Figure 10: A comparision of geocoded groins from VA CUSP and MA data. (A) shows the groins (red lines) from VA CUSP overlaid with VBMP imagery, and (B) shows the groins from MA data overlaid with MA orthoimagery.

is not directly aligned in all cases, the three-meter buffer applied may have been insufficient to capture the contextual pixels required to accurately classify all cases; this is in contrast to Massachusetts (Figure 10B) where such errors did not exist across most observations. Because the overall model accuracy was significantly higher (up to 83% overall accuracy) when Massachusetts data was included, it is feasible that our validation is understating the overall accuracy of the model in Virginia simply because our validation and calibration data itself has apparent errors. Future testing across separately digitized datasets could help to test this hypothesis; alternatively, work to correct the errors across the VA CUSP dataset could bear useful fruit for this and other similar initiatives.

4.4. Scale of Classification

416

417

418

419

The primary unit of classification in this work was the pixel - i.e., we sought to train an algorithm to take in an image tile, and output which pixels belonged to each of four classes. In practice, this level of spatial precision is higher than what may be required for some tasks: i.e., if one has a shoreline defined by a line feature, one could break that shoreline up with an object-based strategy, and then classify each resultant subset of the shoreline as belonging to





Figure 11: Example of features from VA CUSP not fully aligned with the imagery. On the left is a riprap, and on the right is two breakwater structures from VA CUSP.

a given class (rather than classify each pixel). More broadly, many small errors - especially errors on the landward side of a given coastal feature - may not negatively influence decision making. Future work exploring the semantic definition of shoreline, and how that may interrelate with the appropriate scale and unit of observation for automated approaches to classification, could provide a fruitful pathway forward.

4.5. pyShore: A semi-automated toolkit for shoreline structure classification in ArcGIS

A core motivation for this work is to mitigate the total amount of time required to digitize vast amounts of shoreline; as noted in our introduction, today shoreline mapping processes take around a decade (CCRM, 2019; Fontenault et al., 2013). While future iterations of the work presented here may enable a fully automated pipeline for shoreline feature detection, the accuracy of the presented approach renders it best suited to a semi-automated approach in which human experts correct the output of the automated procedures. To enable this, here we present *pyShore*, a semi-automated toolkit for shoreline structure classification in the ArcGIS Pro (ESRI, 2022) software package.

This tool is designed to take in two files - imagery and a definition of shoreline - and output for each pixel in the shoreline a best estimate of the type of shoreline feature present. Using PAN-Resnet18 as an example, these files are passed into the pre-trained PAN-Resnet18 model presented in this work, specifically the best performing NAIP 4-band model with 72% overall accuracy.¹ The user must set a single parameter - buffer distance.

The full workflow of the tool follows a multiple step procedure in which (see Fig. 12):

- 1. The user defines a working folder (F) in which to save all processing and result data.
- 2. The user defines a folder with all source imagery in a georeferenced *geoTiff* format (*Fimg*).
- 3. The user defines a single geometry file (i.e., shapefile) that defines the geographic locations of shoreline within

432

433

434

435

436

437

¹Of note, depending on the spatial resolution of input imagery, for some users it may make sense to implement one of the VA or MA orthoimagery pre-trained models. We provide an optional download of the best performing weights for these data to enable such an analysis.

pyShore: A deep learning toolkit for shoreline structure mapping with high-resolution orthographic imagery and convolutional neural networks

- the provided imagery (S).
- 44. The user provides a buffer distance (B), or the distance from the shoreline that should be extracted from the imagery to serve as the target for the classification.
- 5. All images in folder Fimg are cut into non-overlapping 256×256 patches (defined as P) suitable for input into the trained PAN model architecture.
- 6. Taking in all patches P, line S, and buffer B, we identify the image patches in P that have overlap with buffered line S; image patches with no overlap and dimension smaller than 256×256 are discarded.
- 7. Each patch is subjected to a forward pass through the Resnet-18-based PAN trained in this paper, creating an output (O) of the same dimensions (256×256) in which each pixel is classified as one of four classes (four shoreline structures).
- 8. Pixels intersecting with the shoreline feature (S) with buffer distance, B, are extracted from output, O, and then vectorized to provide a final shoreline output.
- Figure 12 summarizes the workflow of image processing, prediction, and post-processing. In addition to outputting
 the shoreline, a metric of confidence is generated to help guide user efforts, i.e., identifying the areas where the algorithm was least confident in its prediction so a human coder may select those areas for editing during a post-processing
 stage. This confidence level for each line segment (represented as a 3-meter buffered polygon) is generated by:

Confidence =
$$\frac{1}{n} \sum_{i=1}^{n} \frac{X_i - X_{min}}{X_{max} - X_{min}}$$
(8)

where X_i is the absolute score the PAN-Resnet18 estimates for the class a given pixel (i) was predicted as. X_{min} and X_{max} are the smallest and largest such estimate across all pixels in a target region. To calculate the confidence value for a given 3-meter buffered polygon, we define n as the set of pixels a buffered polygon overlaps. The confidence value for any target polygon is defined as the average confidence value of pixels in the layer that overlap with the polygon.

4.6. Contributions to the Literature

The work presented in this paper provides four core contributions. First, we introduce the first application of shoreline structure classification and mapping using deep learning techniques with pixel-scale localization, illustrating that
accuracy of up to 83% is possible with contemporary deep learning techniques. Second, we provide some of the first
evidence of the value of near-infrared spectral data in the context of deep learning for shoreline feature identification,
specifically finding that NIR information can help reduce the computational complexity of algorithms required for generating sufficiently accurate estimates for use in semi-automated workflows. Third, we introduce a toolkit to employ a
deep learning framework within the ArcGIS Pro environment to facilitate rapid shoreline feature identification. Fourth,

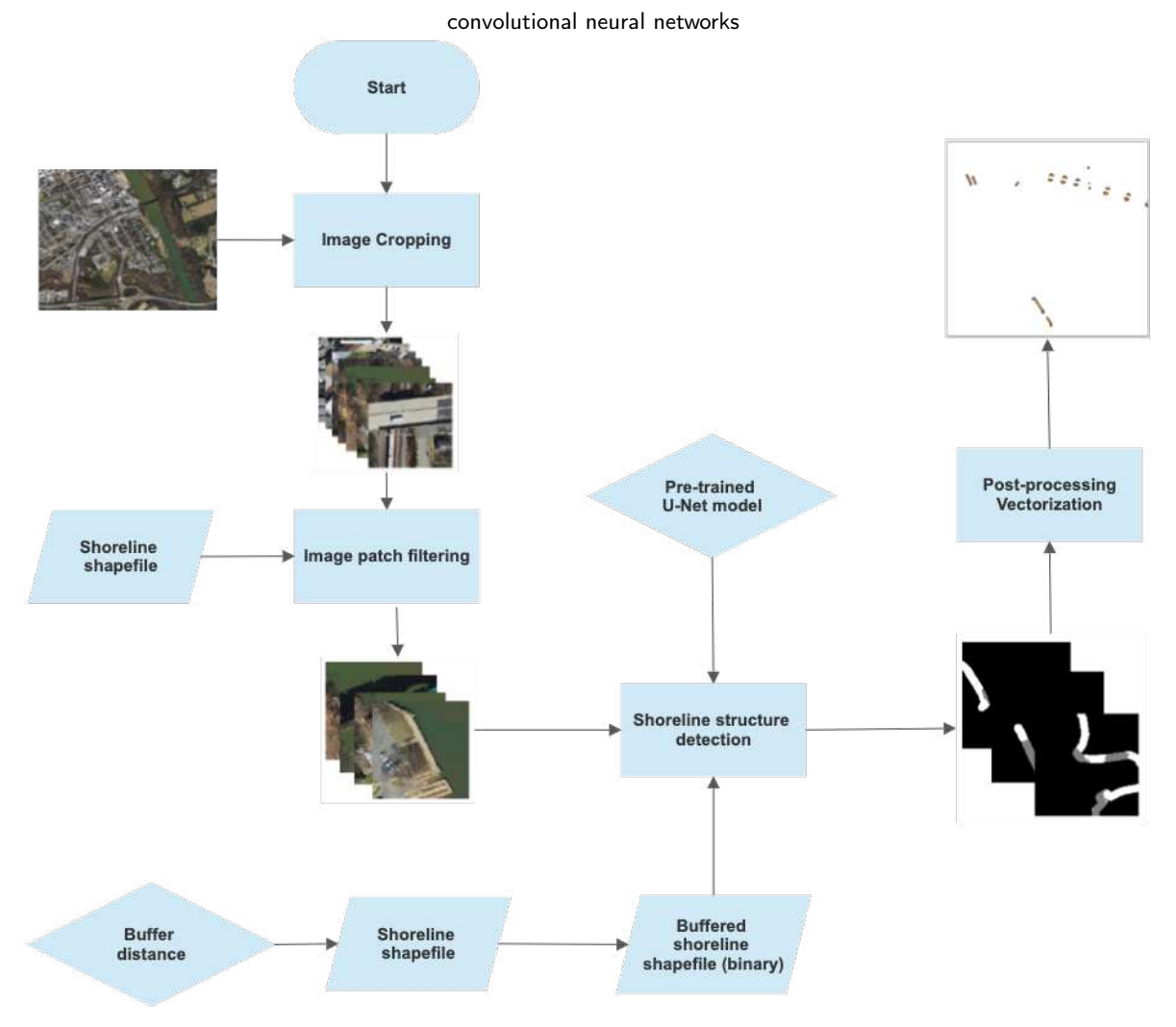


Figure 12: Workflow of shoreline structure detection using the pyShore ArcGIS Pro toolkit.

from a shoreline management and sedimentation modeling perspective, the generated shoreline structure locations and types would be used as input for a shoreline management model (Nunez et al., 2022) which provides recommendations for the best management practices for defended and undefended shorelines. These contributions will enable more rapid digitization of shoreline features than was previously possible, aiding in increasing the rate at which shoreline maps can be generated and updated.

5. Conclusion

474

475

476

Accurate and precise low-cost shoreline structure mapping has the potential to improve the baseline information supporting shoreline management, thus improving the decision-making capacity of local, state, and national governments. Today, shoreline structure mapping is a challenging task due to requirements for in-situ data collection, manual

convolutional neural networks

image digitization, and the inevitability of concurrent shoreline change during years-long production processes.

In this paper, we sought to explore the capability of convolutional neural network architectures to identify shoreline structures from remotely sensed imagery. This study provides (1) an initial benchmark accuracy (72%) for deep
learning-based shoreline structure localization in Virginia (82% across a combination of Virginia and Massachusetts
datasets), and (2) a computationally efficient toolkit that can be deployed in desktop environments which harnesses
the proposed method for applied use. These findings, and the related toolkit provide a new method for local and state
governments in the United States to generate shoreline inventories, and improve the management of coastal resources
and infrastructure.

6. Acknowledgments

The authors acknowledge William & Mary Research Computing for providing computational resources and technical support that have contributed to the results reported within this paper. URL: https://www.wm.edu/it/rc.

convolutional neural networks

488 Code availability section

- Name of the code/library
- 490 Contact: zlv@wm.edu
- Hardware requirements: Python 3.7.10
- 492 Program language: Python
- Software required: ArcGIS Pro 2.3.0
- 494 Github size: 107MB
- The source codes are available for downloading at the link: https://github.com/MirandaLv/pyShore

496 References

- 497 An, Y., Guo, J., Ye, Q., Childs, C., Walsh, J., Dong, R., 2021. Deep convolutional neural network for automatic fault recognition from
- 3d seismic datasets. Computers & Geosciences 153, 104776. URL: https://www.sciencedirect.com/science/article/pii/
- 499 S0098300421000807, doi:https://doi.org/10.1016/j.cageo.2021.104776.
- 500 Aravena Pelizari, P., Geiß, C., Aguirre, P., Santa María, H., Merino Peña, Y., Taubenböck, H., 2021. Automated building characterization
- 501 for seismic risk assessment using street-level imagery and deep learning. ISPRS Journal of Photogrammetry and Remote Sensing 180,
- 502 370-386. URL: https://www.sciencedirect.com/science/article/pii/S0924271621001817, doi:https://doi.org/10.1016/
- j.isprsjprs.2021.07.004.
- Ayala, C., Sesma, R., Aranda, C., Galar, M., 2021. A deep learning approach to an enhanced building footprint and road detection in high-resolution
- satellite imagery. Remote Sensing 13. URL: https://www.mdpi.com/2072-4292/13/16/3135, doi:10.3390/rs13163135.
- Bagli, S., Soille, P., 2004. Automatic delineation of shoreline and lake boundaries from landsat satellite images. Proceedings of initial ECO-
- IMAGINE GI and GIS for Integrated Coastal Management.
- 508 Berman, M., Hershner, C., 1999. Development of guidelines for generating shoreline situation reports establishing protocols for data collection and
- ${\it dissemination. Available on line: http://ccrm.vims.edu/gis_data_maps/shoreline_inventories/shoreline_situation.pdf.}$
- Berman, M., Hershner, C., Angst, K., Killeen, S., Nunez, K., Rudnicky, T., Schatt, D., Stanhope, D., Weiss, D., 2013. Delaware shoreline inventory:
- Rehoboth bay, comprehensive coastal inventory program. Center for Coastal Resources Management Virginia Institute of Marine Science, Col-
- lege of William and Mary, Gloucester Point, Virginia, 23062. https://www.vims.edu/ccrm/research/inventory/delaware/index.
- 513 php.
- Bhil, K., Shindihatti, R., Mirza, S., Latkar, S., Ingle, Y.S., Shaikh, N.F., Prabu, I., Pardeshi, S.N., 2022. Recent progress in object detection in
- satellite imagery: A review, in: Aurelia, S., Hiremath, S.S., Subramanian, K., Biswas, S.K. (Eds.), Sustainable Advanced Computing, Springer
- Singapore, Singapore. pp. 209–218.
- Bhosle, K., Musande, V., 2019. Evaluation of deep learning cnn model for land use land cover classification and crop identification using hy-
- perspectral remote sensing images. Journal of the Indian Society of Remote Sensing 47, 1949–1958. URL: https://doi.org/10.1007/
- s12524-019-01041-2, doi:10.1007/s12524-019-01041-2.
- Breiman, L., 2001. Random forests. Machine Learning 45, 5–32. doi:10.1023/A:1010950718922.
- Brewer, E., Lin, J., Kemper, P., Hennin, J., Runfola, D., 2021. Predicting road quality using high resolution satellite imagery: A transfer learning
- approach. PLOS ONE 16, 1-18. URL: https://doi.org/10.1371/journal.pone.0253370, doi:10.1371/journal.pone.0253370.

- Brewer, E., Lin, J., Runfola, D., 2022. Susceptibility & defense of satellite image-trained convolutional networks to backdoor attacks. Information
- Sciences 603, 244–261. doi:10.1016/J.INS.2022.05.004.
- 525 CCRM, 2019. Virginia shoreline inventory database. Center for Coastal Resources Management, Virginia Institute of Marine Science, College of
- William and Mary, Gloucester Point. http://www.vims.edu/ccrm/research/inventory/index.php.
- 527 Chen, L.C., Papandreou, G., Kokkinos, I., Murphy, K., Yuille, A.L., 2016. Deeplab: Semantic image segmentation with deep convolutional nets,
- atrous convolution, and fully connected crfs. URL: https://arxiv.org/abs/1606.00915, doi:10.48550/ARXIV.1606.00915.
- 529 Chen, X., Xiang, S., Liu, C.L., Pan, C.H., 2014. Vehicle detection in satellite images by hybrid deep convolutional neural networks. IEEE Geoscience
- and Remote Sensing Letters 11, 1797–1801. doi:10.1109/LGRS.2014.2309695.
- 531 Cheng, G., Han, J., 2016. A survey on object detection in optical remote sensing images. ISPRS Journal of Photogrammetry and Remote Sensing 117,
- 532 11-28. URL: https://www.sciencedirect.com/science/article/pii/S0924271616300144, doi:https://doi.org/10.1016/j.
- isprsjprs.2016.03.014.
- 534 Di, K., Wang, J., Ma, R., Li, R., 2003. Automatic shoreline extraction from high resolution ikonos satellite imagery. ASPRS Annual Conference
- Proceedings .
- bigitalGlobe, 2018. Digitalglobe. Retrieved from: https://www.digitalglobe.com/.
- Du, J., Shen, J., Bilkovic, D.M., Hershner, C.H., Sisson, M., 2016. A numerical modeling approach to predict the effect of a storm surge barrier
- on hydrodynamics and long-term transport processes in a partially mixed estuary. Estuaries and Coasts 2016 40:2 40, 387–403. URL: https:
- //link.springer.com/article/10.1007/s12237-016-0175-0, doi:10.1007/S12237-016-0175-0.
- Eboigbe, M.A., Ugwuoti, A.I., Sam, A.A., 2020. The effectiveness of the semi-automatic technique in extracting shoreline from digital elevation
- models for sustainable development in africa. European Journal of Environment and Earth Sciences 1(4). URL: https://www.ej-geo.org/
- index.php/ejgeo/article/view/48, doi:10.24018/ejgeo.2020.1.4.48.
- Enwright, N.M., Griffith, K.T., Osland, M.J., 2016. Barriers to and opportunities for landward migration of coastal wetlands with sea-level rise.
- Frontiers in Ecology and the Environment 14, 307–316. doi:10.1002/FEE.1282/FULLPDF.
- ESRI, 2022. ArcGIS Pro 2.3.0. Redlands, CA: Environmental Systems Research Institute.
- Etten, A.V., Hogan, D., Martinez-Manso, J., Shermeyer, J., Weir, N., Lewis, R., 2021. The multi-temporal urban development spacenet dataset.
- CoRR abs/2102.04420. URL: https://arxiv.org/abs/2102.04420, arXiv:2102.04420.
- Fontenault, J., Vinhateiro, N., Knee, K., 2013. Mapping and analysis of privately-owned coastal structures along the massachusetts shoreline.
- https://www.mass.gov/doc/mapping-and-analysis-of-privately-owned-coastal-structures-along-the-ma-shoreline/
- 550 download
- 551 Ghorai, D., Mahapatra, M., 2020. Extracting shoreline from satellite imagery for gis analysis. Remote Sens Earth Syst Sci 3, 13-22. URL:
- https://doi.org/10.1007/s41976-019-00030-w.
- 553 Gittman, R.K., Fodrie, F.J., Popowich, A.M., Keller, D.A., Bruno, J.F., Currin, C.A., Peterson, C.H., Piehler, M.F., 2015. Engineer-
- ing away our natural defenses: an analysis of shoreline hardening in the us. Frontiers in Ecology and the Environment 13, 301–307.
- URL: https://onlinelibrary.wiley.com/doi/full/10.1890/150065https://onlinelibrary.wiley.com/doi/abs/10.1890/
- 556 150065https://esajournals.onlinelibrary.wiley.com/doi/10.1890/150065, doi:10.1890/150065.
- GLAD, 2018. Landsat analysis ready data. Accessed on July 2022: https://glad.umd.edu/.
- 558 Gong, P., Wang, J., Yu, L., Zhao, Y., Zhao, Y., Liang, L., Niu, Z., Huang, X., Fu, H., Liu, S., Li, C., Li, X., Fu, W., Liu, C., Xu, Y., Wang, X., Cheng,
- 560 Shi, T., Zhu, M., Chen, Y., Yang, G., Tang, P., Xu, B., Giri, C., Clinton, N., Zhu, Z., Chen, J., Chen, J., 2013. Finer resolution observation and

- monitoring of global land cover: first mapping results with landsat tm and etm+ data. International Journal of Remote Sensing 34, 2607–2654.
- 562 URL: https://www.tandfonline.com/doi/full/10.1080/01431161.2012.748992, doi:10.1080/01431161.2012.748992.
- 600 Goodman, S., Ben Yishay, A., Runfola, D., 2021. A convolutional neural network approach to predict non-permissive environments from moderate-
- resolution imagery. Transactions in GIS 25, 674-691. URL: https://onlinelibrary.wiley.com/doi/10.1111/tgis.12661, doi:10.
- 565 1111/tgis.12661.
- 656 Guirado, E., Tabik, S., Alcaraz-Segura, D., Cabello, J., Herrera, F., 2017. Deep-learning versus obia for scattered shrub detection with google
- earth imagery: Ziziphus lotus as case study. Remote Sensing 9, 1220. URL: http://www.mdpi.com/2072-4292/9/12/1220, doi:10.3390/
- rs9121220.
- Guirado, E., Tabik, S., L. Rivas, M., Alcaraz-Segura, D., Herrera, F., 2019. Whale counting in satellite and aerial images with deep learning.
- Scientific Reports 9. doi:10.1038/s41598-019-50795-9.
- 571 He, K., Gkioxari, G., Dollár, P., Girshick, R.B., 2017. Mask R-CNN. CoRR abs/1703.06870. URL: http://arxiv.org/abs/1703.06870,
- 572 arXiv:1703.06870.
- Hill, K., 2015. Coastal infrastructure: a typology for the next century of adaptation to sea-level rise. Frontiers in Ecology and the Environment 13,
- 468-476. URL: https://onlinelibrary.wiley.com/doi/full/10.1890/150088https://onlinelibrary.wiley.com/doi/abs/
- 575 10.1890/150088https://esajournals.onlinelibrary.wiley.com/doi/10.1890/150088, doi:10.1890/150088.
- 576 Kikaki, K., Kakogeorgiou, I., Mikeli, P., Raitsos, D.E., Karantzalos, K., 2022. Marida: A benchmark for marine debris detection from sentinel-2
- remote sensing data. PLOS ONE 17, e0262247. URL: https://journals.plos.org/plosone/article?id=10.1371/journal.pone.
- 578 0262247, doi:10.1371/JOURNAL.PONE.0262247.
- Krizhevsky, A., Sutskever, I., Hinton, G., 2012. Imagenet classification with deep convolutional neural networks. Neural Information Processing
- 580 Systems 25. doi:10.1145/3065386.
- Kuleli, T., Guneroglu, A., Karsli, F., Dihkan, M., 2011. Automatic detection of shoreline change on coastal ramsar wetlands of turkey. Ocean En-
- gineering 38, 1141-1149. URL: https://www.sciencedirect.com/science/article/pii/S0029801811000874, doi:https://doi.
- org/10.1016/j.oceaneng.2011.05.006.
- Kumar, L., Afzal, M.S., Afzal, M.M., 2020. Mapping shoreline change using machine learning: a case study from the eastern indian coast. Acta
- беорнувіса , 1–17.
- Li, H., Wang, C., Cui, Y., Hodgson, M., 2021. Mapping salt marsh along coastal south carolina using u-net. ISPRS Journal of Photogrammetry and
- Remote Sensing 179, 121–132. doi:10.1016/J.ISPRSJPRS.2021.07.011.
- Li, H., Xiong, P., An, J., Wang, L., 2018. Pyramid attention network for semantic segmentation. URL: https://arxiv.org/abs/1805.10180,
- doi:10.48550/ARXIV.1805.10180.
- 590 Liu, H., Wang, L., Sherman, D.J., Wu, Q., Su, H., 2011. Algorithmic foundation and software tools for extracting shoreline features from remote
- sensing imagery and lidar data. Journal of Geographic Information System. Vol.3, No.2.
- Liu, M., Fu, B., Xie, S., He, H., Lan, F., Li, Y., Lou, P., Fan, D., 2021. Comparison of multi-source satellite images for classifying marsh vegetation
- using deeplabv3 plus deep learning algorithm. Ecological Indicators 125, 107562. URL: https://www.sciencedirect.com/science/
- article/pii/S1470160X21002272, doi:https://doi.org/10.1016/j.ecolind.2021.107562.
- Loos, E., Niemann, K., 2002. Shoreline feature extraction from remotely-sensed imagery, in: IEEE International Geoscience and Remote Sensing
- Symposium, pp. 3417–3419 vol.6. doi:10.1109/IGARSS.2002.1027201.
- Lundberg, S., Lee, S.I., 2017. A unified approach to interpreting model predictions. URL: https://arxiv.org/abs/1705.07874, doi:10.
- 598 48550/ARXIV.1705.07874.

- Mason, D., Davenport, I., 1996. Accurate and efficient determination of the shoreline in ers-1 sar images. IEEE Transactions on Geoscience and
- Remote Sensing 34, 1243–1253. doi:10.1109/36.536540.
- 601 McAllister, E., Payo, A., Novellino, A., Dolphin, T., Medina-Lopez, E., 2022a. Multispectral satellite imagery and machine learning for the
- extraction of shoreline indicators. Coastal Engineering 174, 104102. URL: https://www.sciencedirect.com/science/article/pii/
- 603 S0378383922000229, doi:https://doi.org/10.1016/j.coastaleng.2022.104102.
- McAllister, E., Payo, A., Novellino, A., Dolphin, T., Medina-Lopez, E., 2022b. Multispectral satellite imagery and machine learning for the
- extraction of shoreline indicators. Coastal Engineering 174, 104-102. URL: https://www.sciencedirect.com/science/article/pii/
- 606 S0378383922000229, doi:https://doi.org/10.1016/j.coastaleng.2022.104102.
- MGS, 2000. High resolution shoreline map data for tidewater maryland. Maryland Geological Survey http://www.mgs.md.gov/coastal_
- 608 geology.
- Najjar, R.G., Pyke, C.R., Adams, M.B., Breitburg, D., Hershner, C., Kemp, M., Howarth, R., Mulholland, M.R., Paolisso, M., Secor, D., Sell-
- ner, K., Wardrop, D., Wood, R., 2010. Potential climate-change impacts on the chesapeake bay. Estuarine, Coastal and Shelf Science 86,
- 611 1-20. URL: https://www.sciencedirect.com/science/article/pii/S0272771409004582, doi:https://doi.org/10.1016/j.
- ecss.2009.09.026.
- Narayan, A., Tuci, E., Labrosse, F., Alkilabi, M.H.M., 2017. Road detection using convolutional neural networks. Proceedings of the 14th Euro-
- pean Conference on Artificial Life ECAL 2017, 314-321URL: https://www.mitpressjournals.org/doi/abs/10.1162/isal_a_053,
- doi:10.7551/ecal_a_053.
- 616 Niculescu, S., Bengoufa, S., Mihoubi, M., Belkessa, R., Abbad, K., 2021. ROCKY SHORELINE EXTRACTION USING A DEEP
- 617 LEARNING MODEL AND OBJECT-BASED IMAGE ANALYSIS. International Archives of the Photogrammetry, Remote Sensing
- and Spatial Information Sciences XLIII-B3-2021, 23-29. URL: https://hal.archives-ouvertes.fr/hal-03274256, doi:10.5194/
- isprs-archives-XLIII-B3-2021-23-2021.
- NOAA, 2018. Sentinel. Retrieved from: https://sentinel.esa.int/web/sentinel/home.
- NOAA, 2021a. Noaa continually updated shoreline product (cusp). Accessed on March 2022: https://shoreline.noaa.gov/data/
- datasheets/cusp.html.
- NOAA, 2021b. Noaa's continually updated shoreline product (cusp). Accessed on March 2022: https://www.ngs.noaa.gov/INFO/
- OnePagers/CUSP_One-Pager.pdf.
- Nunez, K., Rudnicky, T., Mason, P., Tombleson, C., Berman, M., 2022. A geospatial modeling approach to assess site suitability of living shorelines
- and emphasize best shoreline management practices. Ecological Engineering 179, 106617. doi:10.1016/J.ECOLENG.2022.106617.
- Nunez, K., Zhang, Y.J., Herman, J., Reay, W., Hershner, C., 2020. A multi-scale approach for simulating tidal marsh evolution. Ocean
- 628 Dynamics 2020 70:9 70, 1187-1209. URL: https://link.springer.com/article/10.1007/s10236-020-01380-6, doi:10.1007/
- S10236-020-01380-6.
- OCM-Partners, 2022. 2018 virginia naip digital ortho photo imagery. NOAA National Centers for Environmental Information. https://www.
- fisheries.noaa.gov/inport/item/58386.
- Palaseanu-Lovejoy, M., Danielson, J.J., Thatcher, C.A., Foxgrover, A.C., Barnard, P.L., Brock, J., Young, A., 2016. Automatic delineation of
- seacliff limits using lidar-derived high-resolution dems in southern california. Journal of Coastal Research, 162–173.doi:10.2112/SI76-014.
- Paszke, A., Chaurasia, A., Kim, S., Culurciello, E., 2016. Enet: A deep neural network architecture for real-time semantic segmentation. CoRR
- abs/1606.02147. URL: http://arxiv.org/abs/1606.02147, arXiv:1606.02147.
- Payo, A., Antelo, B.J., Hurst, M., Palaseanu-Lovejoy, M., Williams, C., Jenkins, G., Lee, K., Favis-Mortlock, D., Barkwith, A., Ellis, M.A., 2018.

- Development of an automatic delineation of cliff top and toe on very irregular planform coastlines (cliffmetrics v1.0). Geosci. Model Dev., 11,
- 4317-4337.doi:https://doi.org/10.5194/gmd-11-4317-2018.
- Phillips, S., McGee, B., 2014. The economic benefits of cleaning up the Chesapeake. Technical Report. Chesapeake Bay Program. URL: https://
- 640 www.cbf.org/news-media/features-publications/reports/economic-benefits-of-cleaning-up-the-chesapeake-bay/.
- Prathap, G., Afanasyev, I., 2018. Deep learning approach for building detection in satellite multispectral imagery, in: 2018 International Conference
- on Intelligent Systems (IS), pp. 461–465. doi:10.1109/IS.2018.8710471.
- Rezatofighi, H., Tsoi, N., Gwak, J., Sadeghian, A., Reid, I., Savarese, S., 2019. Generalized intersection over union: A metric and a loss for bounding
- box regression. URL: https://arxiv.org/abs/1902.09630, doi:10.48550/ARXIV.1902.09630.
- Roberts, J., Mwangi, R., Mukabi, F., Njui, J., Nzioka, K., Ndambiri, J., Bispo, P., Espirito-Santo, F., Gou, Y., Johnson, S., Louis, V., Pacheco-
- Pascagaza, A., Rodriguez-Veiga, P., Tansey, K., Upton, C., Robb, C., Balzter, H., 2022. Pyeo: A python package for near-real-time for-
- est cover change detection from earth observation using machine learning. Computers & Geosciences 167, 105192. URL: https://www.
- 648 sciencedirect.com/science/article/pii/S0098300422001455, doi:https://doi.org/10.1016/j.cageo.2022.105192.
- Ronneberger, O., Fischer, P., Brox, T., 2015. U-net: Convolutional networks for biomedical image segmentation. Lecture Notes in Computer
- Science (including subseries Lecture Notes in Artificial Intelligence and Lecture Notes in Bioinformatics) 9351, 234–241. URL: https://
- 651 link.springer.com/chapter/10.1007/978-3-319-24574-4_28, doi:10.1007/978-3-319-24574-4_28.
- Runfola, D., 2022. Computational geography. The Geographic Information Science & Technology Body of Knowledge (1st Quarter 2022 Edition),
- John P. Wilson (Ed.). URL: https://gistbok.ucgis.org/bok-topics/computational-geography, doi:10.22224/gistbok/2022.
- 654 1.7.
- Runfola, D., Anderson, A., Baier, H., Crittenden, M., Dowker, E., Fuhrig, S., Goodman, S., Grimsley, G., Layko, R., Melville, G., Mulder, M.,
- Oberman, R., Panganiban, J., Peck, A., Seitz, L., Shea, S., Slevin, H., Youngerman, R., Hobbs, L., 2020. geoboundaries: A global database
- of political administrative boundaries. PLOS ONE 15, e0231866. URL: https://journals.plos.org/plosone/article?id=10.1371/
- journal.pone.0231866, doi:10.1371/JOURNAL.PONE.0231866.
- 659 Runfola, D., Baier, H., Mills, L., Naughton-Rockwell, M., Stefanidis, A., 2022. Deep learning fusion of satellite and social information to estimate
- 660 human migratory flows. Transactions in GIS URL: https://onlinelibrary.wiley.com/doi/full/10.1111/tgis.12953https:
- //onlinelibrary.wiley.com/doi/abs/10.1111/tgis.12953https://onlinelibrary.wiley.com/doi/10.1111/tgis.12953,
- doi:10.1111/TGIS.12953.
- Runfola, D., Stefanidis, A., Baier, H., 2021. Using satellite data and deep learning to estimate educational outcomes in data-sparse en-
- vironments. https://doi.org/10.1080/2150704X.2021.1987575 13, 87-97. URL: https://www.tandfonline.com/doi/abs/10.1080/
- $\textbf{665} \qquad \quad 2150704 \texttt{X}.2021.1987575, \\ doi: 10.1080/2150704 \texttt{X}.2021.1987575.$
- 666 Sekovski, I., Stecchi, F., Mancini, F., Rio, L.D., 2014. Image classification methods applied to shoreline extraction on very high-resolution mul-
- tispectral imagery. International Journal of Remote Sensing 35, 3556–3578. URL: https://doi.org/10.1080/01431161.2014.907939,
- doi:10.1080/01431161.2014.907939, arXiv:https://doi.org/10.1080/01431161.2014.907939.
- Spinosa, A., Ziemba, A., Saponieri, A., Damiani, L., El Serafy, G., 2021. Remote sensing-based automatic detection of shoreline position: A case
- 570 study in apulia region. Journal of Marine Science and Engineering. 9(6). URL: https://www.mdpi.com/2077-1312/9/6/575, doi:10.
- 3390/jmse9060575.
- 572 State of Washington, 2009. Shoreline master programs handbook. URL: https://apps.ecology.wa.gov/publications/SummaryPages/
- 673 1106010.html.
- 574 Stofa, M.M., Zulkifley, M.A., Zaki, S.Z.M., 2020. A deep learning approach to ship detection using satellite imagery. IOP Conference Series: Earth

- and Environmental Science 540, 012049. URL: https://doi.org/10.1088/1755-1315/540/1/012049, doi:10.1088/1755-1315/540/1/012049, doi:10.1088/175-1315/540/1/012049, doi:10.1088/1755-1315/540/1/012049, doi:10.1088/1750/10089, doi:10.1088/1750/10089, doi:10.1088/1750/10089, doi:10.1088/1750/10089, doi:10.1088/1750/1008
- 676 1/012049.
- Tarmizi, N.M., Samad, A.M., Yusop, M.S.M., 2014. Shoreline data extraction from quickbird satellite image using semi-automatic technique, in:
- 678 2014 IEEE 10th International Colloquium on Signal Processing and its Applications, pp. 157–162. doi:10.1109/CSPA.2014.6805739.
- Titus, J., Anderson, K., Cahoon, D., Gesch, D., Gill, S., Gutierrez, B., Thieler, E., William, S., 2009. Coastal sensitivity to sea-level rise: A focus
- on the mid-atlantic region. Accessed on August 2022: https://digital.library.unt.edu/ark:/67531/metadc12028/.
- Toft, J.D., Bilkovic, D.M., Mitchell, M.M., Peyre, M.K.L., 2017. A synthesis of living shoreline perspectives, in: Living Shorelines: The Science
- and Management of Nature-Based Coastal Protection. CRC Press. Taylor & Francis Group, pp. 483–488.
- Tran, S.T., Nguyen, M.H., Dang, H.P., Nguyen, T.T., 2022. Automatic polyp segmentation using modified recurrent residual unet network. IEEE
- Access 10, 65951–65961, doi:10.1109/ACCESS.2022.3184773.
- 685 USGS, 2012. Massgis data color ortho imagery (2008/2009). Retrieved on May 2022: https://www.mass.gov/info-details/
- massgis-data-20082009-aerial-imagery.
- VGIN, 2018. Virginia basemap program orthoimagery: Virginia geographic information network. Accessed on April 2022: https://gismaps.
- vdem.virginia.gov/download/mrsid/.
- Wan, J., Xie, Z., Xu, Y., Chen, S., Qiu, Q., 2021. Da-roadnet: A dual-attention network for road extraction from high resolution satellite imagery.
- 690 IEEE Journal of Selected Topics in Applied Earth Observations and Remote Sensing 14, 6302-6315. doi:10.1109/JSTARS.2021.3083055.
- Wang, Z., Wang, J., Yang, K., Wang, L., Su, F., Chen, X., 2022. Semantic segmentation of high-resolution remote sensing images based on a class
- feature attention mechanism fused with deeplabv3+. Computers & Geosciences 158, 104969. URL: https://www.sciencedirect.com/
- science/article/pii/S0098300421002545, doi:https://doi.org/10.1016/j.cageo.2021.104969.
- 4694 Yang, H.L., Lunga, D., Yuan, J., 2017. Toward country scale building detection with convolutional neural network using aerial images. International
- Geoscience and Remote Sensing Symposium (IGARSS) 2017-July, 870–873. doi:10.1109/IGARSS.2017.8127091.
- Zarillo, G.A., Kelley, J., Larson, V., 2008. A gis based tool for extracting shoreline positions from aerial imagery (beachtools) revised. Coastal and
- 697 Hydraulics Laboratory Engineering Technical Note ERDC/CHL CHETN-IV-73. Vicksburg, MS: U.S. Army Engineer Research and Develop-
- ment Center. URL: http://chl.erdc.usace.army.mil/chetn.